



Bioinspired kirigami metasurfaces as assistive shoe grips

Sahab Babae^{1,2,7}, Simo Pajovic^{1,2,3,7}, Ahmad Rafsanjani^{4,7}, Yichao Shi^{2,3}, Katia Bertoldi⁵✉ and Giovanni Traverso^{1,2,6}✉

Falls and subsequent complications are major contributors to morbidity and mortality, especially in older adults. Here, by taking inspiration from claws and scales found in nature, we show that buckling kirigami structures applied to footwear outsoles generate higher friction forces in the forefoot and transversally to the direction of movement. We identified optimal kirigami designs capable of modulating friction for a range of surfaces, including ice, by evaluating the performance of the dynamic kirigami outsoles through numerical simulations and in vitro friction testing, as well as via human-gait force-plate measurements. We anticipate that lightweight kirigami metasurfaces applied to footwear outsoles could help mitigate the risk of slips and falls in a range of environments.

Falls are a common health problem with a tremendous impact on morbidity and mortality. Falls are ranked as the leading cause of death for older adults¹ and the second leading cause of occupational-related deaths². Musculoskeletal injuries associated with falls include hip fractures, which dramatically increase morbidity and mortality in older adults: nearly half of the patients with hip fractures are unable to return to living independently³, and mortality rates twelve months following hip fracture are 12–37%^{4–7}. Moreover, the direct costs of both fatal and non-fatal falls are estimated to be greater than US\$64 billion per year in the United States^{8–10}. Considering the dangers and costs associated with fall injuries, particularly for high-frequency work injuries involving ice¹¹, efforts have been made to understand and prevent slips and falls^{12–16}, including evaluation of the impact of footwear technologies and the ways in which their basic properties (for example, sole hardness) affect slip resistance^{15–20}. Existing devices such as crampons and snow chains attach to the soles of shoes to increase grip but protrude from the sole at all times and may be tedious to attach and detach. There is thus a need for lightweight dynamic devices that can help prevent slips and falls through friction enhancement of footwear.

Kirigami—the Japanese art of paper cutting—has become a powerful tool for the development of highly flexible devices and transformable structures^{21–24}. Kirigami surfaces are capable of buckling-induced shape transformation from flat sheets to three-dimensional (3D) textured surfaces and have been employed in a broad range of applications, including light manipulation²⁵, energy harvesting²⁶, wearable thermotherapy²⁷, crawling locomotion²⁸, flexible sensors and actuators^{29,30}, stretchable bioprobes³¹, conductive nanocomposites^{32,33} and lithium-ion batteries³⁴. Recently, the anisotropic friction of a kirigami skin enabled locomotion of a crawling soft robot²⁸. Here we report a kirigami-based assistive shoe grip to reduce the risks of slips and falls that is inspired by active friction-control strategies in animals using

claws and scales but recognizes the differences in their niches to where our systems would be applied. We demonstrate the ability to dynamically modulate friction using highly stretchable lightweight kirigami patches comprised of steel sheets perforated with a periodic array of scale-like spikes. The spikes buckle out when stretched, resulting in engagement with the surface of contact and a higher friction force. Through a combination of simulations and experiments, we carefully chose the perforation template so that the resulting spikes are stiff and buckle out at the largest possible angle of attack to maximize engagement of the kirigami grip with the surface in contact. These kirigami patches could serve as a new class of slip-resistant footwear add-ons, which can be tuned to enhance friction between the shoe and specific walking and working surfaces, thereby reducing the risk of slips and falls across many potentially hazardous environments.

Nature is a rich source of inspiration for friction-enhancement designs. Figure 1a shows examples of animals in nature that exploit dynamic modulation of friction for locomotion and gripping. These animals utilize anatomical structures and mechanisms to selectively and transiently increase friction on certain surfaces or in certain situations. For example, cheetahs have semi-retractable claws that increase friction when turning while chasing prey and climbing³⁵. The sharp claws of oxpeckers point in opposing directions to provide a strong grip and stable positioning while riding on the backs of larger mammals ranging from cattle to rhinoceroses³⁶. Snakes orient their scales to increase friction anisotropy and propel themselves forward in rectilinear³⁷ and serpentine locomotion³⁸. Inspired by these animals, we developed slip-resistant assistive kirigami grips that can be attached to the soles of the shoes. Figure 1b shows the undeformed and deformed configurations of a steel kirigami shoe grip with concave spikes attached to a shoe sole. During walking, the bending of the shoe soles induces stretching in the patches and causes the spikes to buckle outward from the soles (Supplementary Video 1). Engagement of the spikes with the walking surface results

¹Department of Mechanical Engineering, Massachusetts Institute of Technology, Cambridge, MA, USA. ²Department of Chemical Engineering and Koch Institute for Integrative Cancer Research, Massachusetts Institute of Technology, Cambridge, MA, USA. ³Department of Mechanical and Industrial Engineering, University of Toronto, Toronto, Ontario, Canada. ⁴Department of Materials, ETH Zurich, Zurich, Switzerland. ⁵John A. Paulson School of Engineering and Applied Sciences, Harvard University, Cambridge, MA, USA. ⁶Division of Gastroenterology, Department of Medicine, Brigham and Women's Hospital, Harvard Medical School, Boston, MA, USA. ⁷These authors contributed equally: Sahab Babae, Simo Pajovic, Ahmad Rafsanjani. ✉e-mail: bertoldi@seas.harvard.edu; cgt20@mit.edu

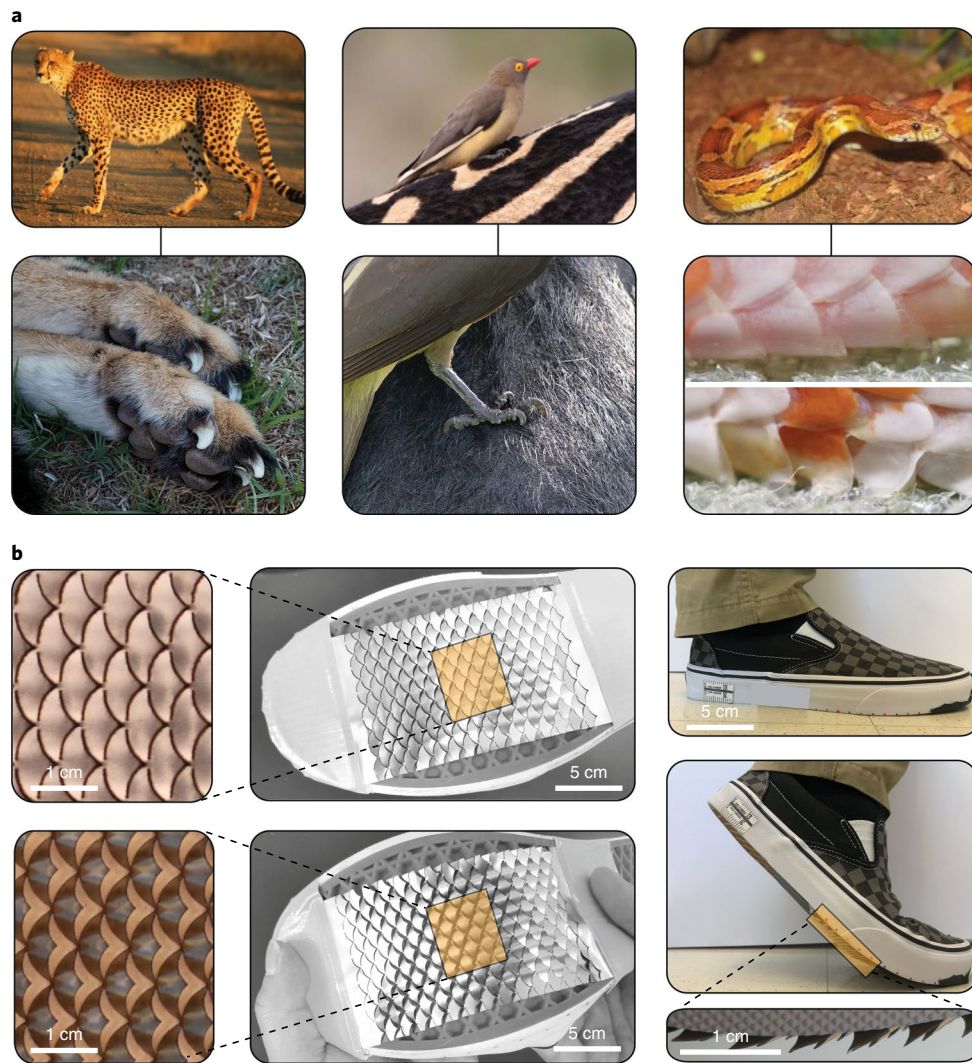


Fig. 1 | Kirigami shoe grip for the dynamic modulation of friction and prevention of slips and falls. a, Inspiration from friction-enhancing strategies in animals: cheetah with semi-retractable claws³⁵ (left), oxpecker with sharp claws in opposing directions³⁶ (middle) and snake with scales that are oriented to increase friction (right)³⁷. **b**, Kirigami for friction modulation in footwear. Steel kirigami surfaces were attached to the shoe soles (middle). The undeformed (top) and deformed (bottom) configurations of the kirigami shoe grip are illustrated. The spikes are activated (shown in the magnified view, bottom right) through changes in the curvature of the shoe soles during walking to actively enhance the frictional properties between the sole of the shoe and walking surface, and reduce the risk of slips and falls. Panel **a** reproduced with permission from Mukul2u, Wikimedia Commons, under a Creative Commons licence [CC BY 3.0](https://creativecommons.org/licenses/by/3.0/) (top left); Marko Kudjerski, Flickr, under a Creative Commons licence [CC BY 2.0](https://creativecommons.org/licenses/by/2.0/) (bottom left); Derek Keats, Flickr, under a Creative Commons licence [CC BY 2.0](https://creativecommons.org/licenses/by/2.0/) (top and bottom middle); and ref. ³⁷, the Royal Society (bottom right).

in a considerable change in the tribological behaviour of the shoes. The kirigami surfaces were engineered to undergo a reversible shape transformation from flat surfaces (corresponding to low friction) to 3D textured surfaces with popped-up spikes (corresponding to high friction). Kirigami patches allow similarly dynamic friction modulation by remaining flat when the wearer is standing still and transforming to increased friction specifically during walking. The patches thereby improve resistance to slips and falls without the hassle or possible discomfort of obtrusive attachments.

Results

Design of kirigami metasurfaces for dynamic friction modulation. Our kirigami shoe grips are composed of a periodic array of needle-like spikes embedded in stainless steel sheets (with a thickness of 0.051 mm and Young's modulus, $E = 193$ GPa; Supplementary Fig. 1). We considered three different shapes for the cuts—that is, concave, triangular and convex spikes. Note that, for a given cut

shape, each kirigami pattern is characterized by two design parameters: the cut angle (γ) and the dimensionless ratio (δ/l) that defines the ratio between the width of the ligaments separating the cuts (δ) and the characteristic length (l) of the periodic lattice (see the inset in Fig. 2b). By varying these two parameters, one can control the mechanical response of the kirigami patterns^{22,28}. We then used nonlinear finite element analyses (see the Numerical simulations section of Methods) to identify a kirigami patch that exhibits a larger tilting angle (θ) and higher out-of-plane stiffness (K_{33}) for better engagement with the surface in contact while maintaining the actuated configuration of the kirigami patch under the weight of the wearer.

In Fig. 2a, we report the numerical snapshots of unit cells with concave- (left), triangular- (middle) and convex-shaped (right) cuts when subjected to in-plane uniaxial strain ε_{22} . We found that the applied deformation triggers a buckling instability that induces the buckling and pop-up of the spikes in all three patterns.

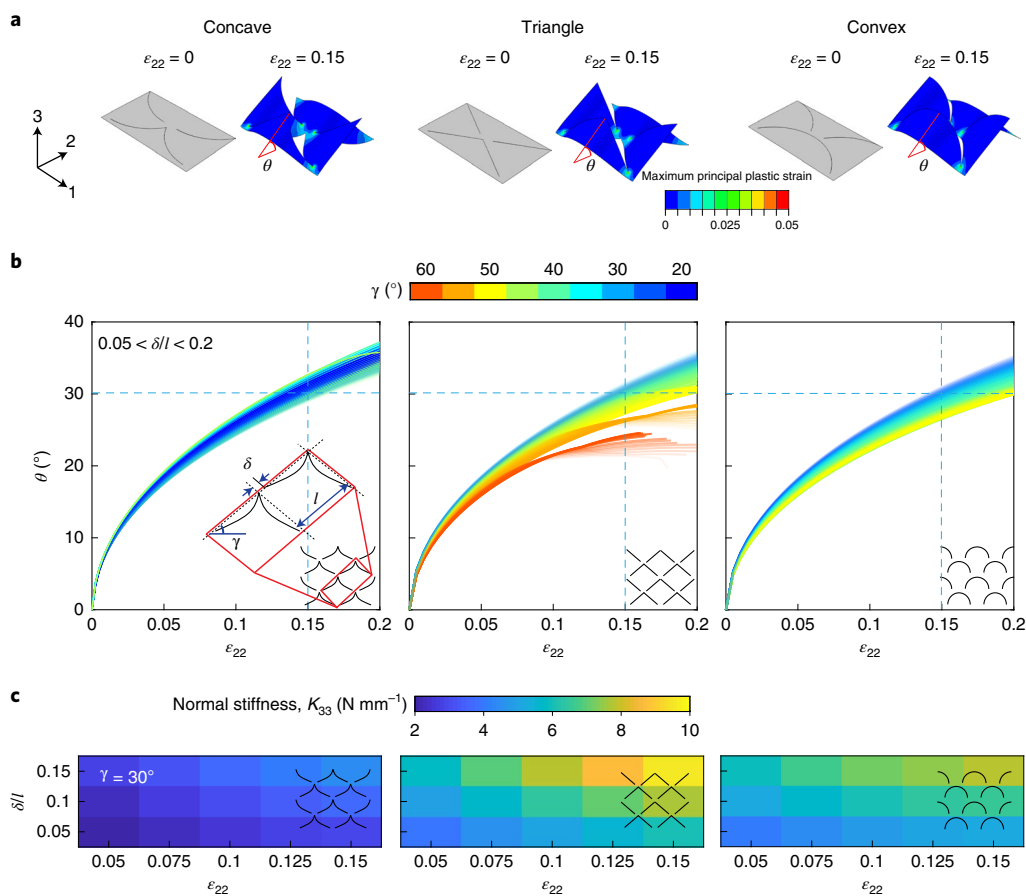


Fig. 2 | Mechanical characterization of the kirigami shoe grips with different spike shapes. **a**, Numerical images showing the configurations of the kirigami unit cells with concave (left), triangular (middle) and convex (right) shapes at different levels of applied uniaxial strains, $\epsilon_{22} = 0$ and 0.15. The colours represent the distribution of the maximum principal plastic strains. **b**, Tilting angle of the spikes plotted as a function of ϵ_{22} for the geometric design parameters γ and δ/l . The dashed vertical and horizontal lines correspond to $\epsilon_{22} = 0.15$ (maximum strain of the average shoe sole over a gait cycle) and θ of about 30° (maximum θ), respectively. Inset, the parameters γ , δ and l are defined (left). **c**, Effect of δ/l on the stiffness in the 33 direction (K_{33}) of the kirigami spikes with concave, triangular and convex shapes with $\gamma = 30^\circ$ as a function of ϵ_{22} .

For $20^\circ < \gamma < 60^\circ$ and $0.05 < \delta/l < 0.2$, we then monitored the evolution of the out-of-plane θ of the spikes as a function of the applied tensile strain ϵ_{22} for each pattern. The data are reported in Fig. 2b, demonstrating that the out-of-plane buckling results in an initial sharp increase in the θ and then an increasing regime, followed by a plateau at higher strains. For example, the θ saturates at $\theta = 22^\circ$ for $\epsilon_{22} \geq 0.1$ for the triangular spikes with $\gamma = 60^\circ$ and $0.05 < \delta/l < 0.2$. The maximum average local strain in the shoe soles induced by changing the curvature of the soles over a gait cycle (see the dashed line in Supplementary Fig. 2) is approximately $\epsilon_{22} = 0.15$. At this strain range, we selected $\gamma = 30^\circ$ as a good candidate for the cutting angle to achieve a maximum θ (θ of about 30°) for all spike shapes (Fig. 2b, blue dashed line).

Next, we constructed finite-element models of kirigami surfaces with different spike shapes at $\gamma = 30^\circ$ and $\delta/l = 0.05, 0.1$ and 0.15 , which were first stretched up to the maximum strain of a typical shoe sole over a gait cycle ($\epsilon_{22} = 0.15$) and then compressed in contact with a rigid plate to estimate the stiffness of the spikes in the out-of-plane direction (K_{33} ; see the Numerical simulations section of Methods and Supplementary Video 2). The data are presented in Fig. 2c, which indicate that $\delta/l = 0.15$ results in maximum K_{33} across different levels of in-plane strain ϵ_{22} for all of the shapes. Thus, having identified $\gamma = 30^\circ$ and $\delta/l = 0.15$ as ideal design parameters, we investigated the effect of spike shape on friction enhancement.

In vitro mechanical characterization of kirigami shoe grips.

Figure 3a shows the undeformed ($\epsilon_{22} = 0$) and buckled ($\epsilon_{22} = 0.15$) configurations of the fabricated steel kirigami patches with $\gamma = 30^\circ$ and $\delta/l = 0.15$ as well as concave, triangular and convex spike shapes. These patches were manufactured by laser-cutting stainless steel sheets (Supplementary Fig. 3 and see the Fabrication of the kirigami patches section of Methods). A custom-built friction testing set-up was retrofitted to a universal testing machine (Instron 5942 series) and used to evaluate the friction force between the kirigami prototypes and different surfaces (Supplementary Fig. 4 and the Friction testing section of Methods).

In Fig. 3b, we report the friction forces (F_f) between kirigami (pre-stretched at $\epsilon_{22} = 0.15$) with different spike shapes and three common walking surfaces—ice (that is, unmelted dry surface), vinyl and hardwood—and compared the results with those measured for flat spikeless steel control patches (Fig. 3b). The controls had the same thickness (0.051 mm) as the kirigami patches. Two primary friction responses were observed among all of the patches and surfaces: (1) smooth sliding, in which the friction force starts with an initial peak (static friction force, F_s) followed by a plateau (kinetic friction force, F_k), and (2) a stick-slip response, in which the friction force varies periodically between a maximum (F_s) and minimum (F_k) force, as presented in the schematic (Fig. 3b, middle insets). The smooth sliding response was observed for hard surfaces such as wood and ice, where the kirigami spikes scratched against the surface

with minimal penetration. The stick–slip response was observed for the semi-hard surface (vinyl), where the spikes appreciably penetrated the surface. Notably, the friction force–displacement curves for all of the kirigami were greater than that of the flat spikeless control patches due to the interactions (scratching or penetrating, confirmed by observing the surfaces after the tests) between the spikes and various surfaces, demonstrating the effectiveness of the kirigami patches in increasing sliding resistance.

Note that some degree of stick–slip friction was almost always observed between the kirigami and the test surfaces. For example, the triangular kirigami exhibited a relatively low degree of stick–slip friction on ice (Fig. 3b, middle), while almost all shapes exhibited a pronounced degree of stick–slip friction on vinyl (Fig. 3b). This behaviour was caused by penetration of the spikes into the test surfaces (stick events), resulting in static friction forces, followed by sharp drops caused by slip events when the force applied by the universal testing machine (equal to the friction force) was large enough to overcome the force of penetration and cause motion again. This is similar to ploughing friction between a soft material and a harder one, where friction is caused by ploughing asperities in the harder material through the softer one³⁹. In our system, the kirigami spikes can be considered as very large asperities ploughing through the softer surfaces such as vinyl. When the softer material accumulates at the tip of the spikes, the kirigami ‘sticks’ until enough force is applied to fracture or slip over the accumulated material. However, in general, ploughing friction is not necessarily related to stick–slip friction; we mention ploughing friction here more as an analogue to the mechanism we believe is at play here.

We further quantified the ability of the kirigami patches to enhance sliding friction by comparing the coefficients of friction of the three walking surfaces to a flat spikeless control surface as shown in Fig. 3c. The static (before a slip event) coefficient of friction (μ), denoted by μ_s , and kinetic coefficient of friction (during motion), denoted by μ_k , were estimated using $\mu_s = F_s/F_n$ and $\mu_k = F_k/F_n$, where F_n is the normal force acting on the patch. In the case of smooth sliding, F_s is the peak friction force, which corresponds to the static friction force that must be overcome before any sliding begins between two stationary surfaces, and F_k is the average kinetic friction force when the surfaces are in relative motion during shearing. For the stick–slip response, F_s and F_k are the maximum and the minimum magnitudes of the measured friction forces, respectively^{40,41}.

We summarized the results in Fig. 3c, demonstrating a significant improvement in both the μ_s and μ_k values for all of the kirigami with different spike shapes compared with their respective controls (bare steel surfaces) across all of the walking surfaces. This difference was especially dramatic on ice, where we observed an enhancement of up to approximately sevenfold in the μ_s and 14-fold in μ_k . Interestingly, the triangular spikes exhibited the lowest improvement, although they had the largest out-of-plane stiffness value ($K_{33} = 11 \text{ N mm}^{-1}$ for $\delta/l = \epsilon_{22} = 0.15$; see the middle heat map in Fig. 2c); while the convex (broad and stiff geometry) and concave spikes (very sharp tip) exhibited higher friction enhancement. Importantly, the concave spikes showed the best performance on

ice by maximizing the kinetic friction coefficient from $\mu_k = 0.020$ to 0.285. The concave spike was therefore selected to manufacture the final kirigami prototypes and study the friction response of kirigami by arranging the spikes in different patterns and directions.

Kirigami shoe grips with varying arrangements of spikes. Next, the effect of spike arrangement on the frictional properties of the kirigami was experimentally investigated. We manufactured steel kirigami patches with five different spatial distributions of concave-shaped spikes—that is, unidirectional (arrangement 1), three-column (arrangement 2), alternating rows (arrangement 3), chequered (arrangement 4) and mirror (arrangement 5)—all of which are illustrated in Fig. 3d and Supplementary Fig. 5. Similarly, we tested these by pulling the pre-stretched kirigami ($\epsilon_{22} = 0.15$) on a test surface (see the Friction testing section of Methods). The friction force–displacement responses between the kirigami and ice with a dry surface are presented in Fig. 3e. Interestingly, all of the kirigami demonstrated enhanced frictional properties in comparison to the control spikeless patch, showing smooth sliding for ice (data for hardwood and vinyl surfaces are presented in Supplementary Fig. 6). We also computed the friction coefficients for different kirigami arrangements, finding significant increases in the μ_s (fivefold) and μ_k (15-fold) on average for all of the arrangements with respect to the control for ice (Fig. 3f). One would expect that arrangement 1 should have the highest μ_s and μ_k values, as all of the spikes are pointing in the same direction, thereby dissipating the most possible energy for a fixed number of spikes because they should all be penetrating into the surface; however, this was not the case experimentally. This is due to a slight flattening of the spike tips as they are pressed against the surface, which decreases the ability of the forward-pointing spikes (that is, pointing in the direction of displacement) to penetrate into the surface and results in a similar friction response for all arrangements.

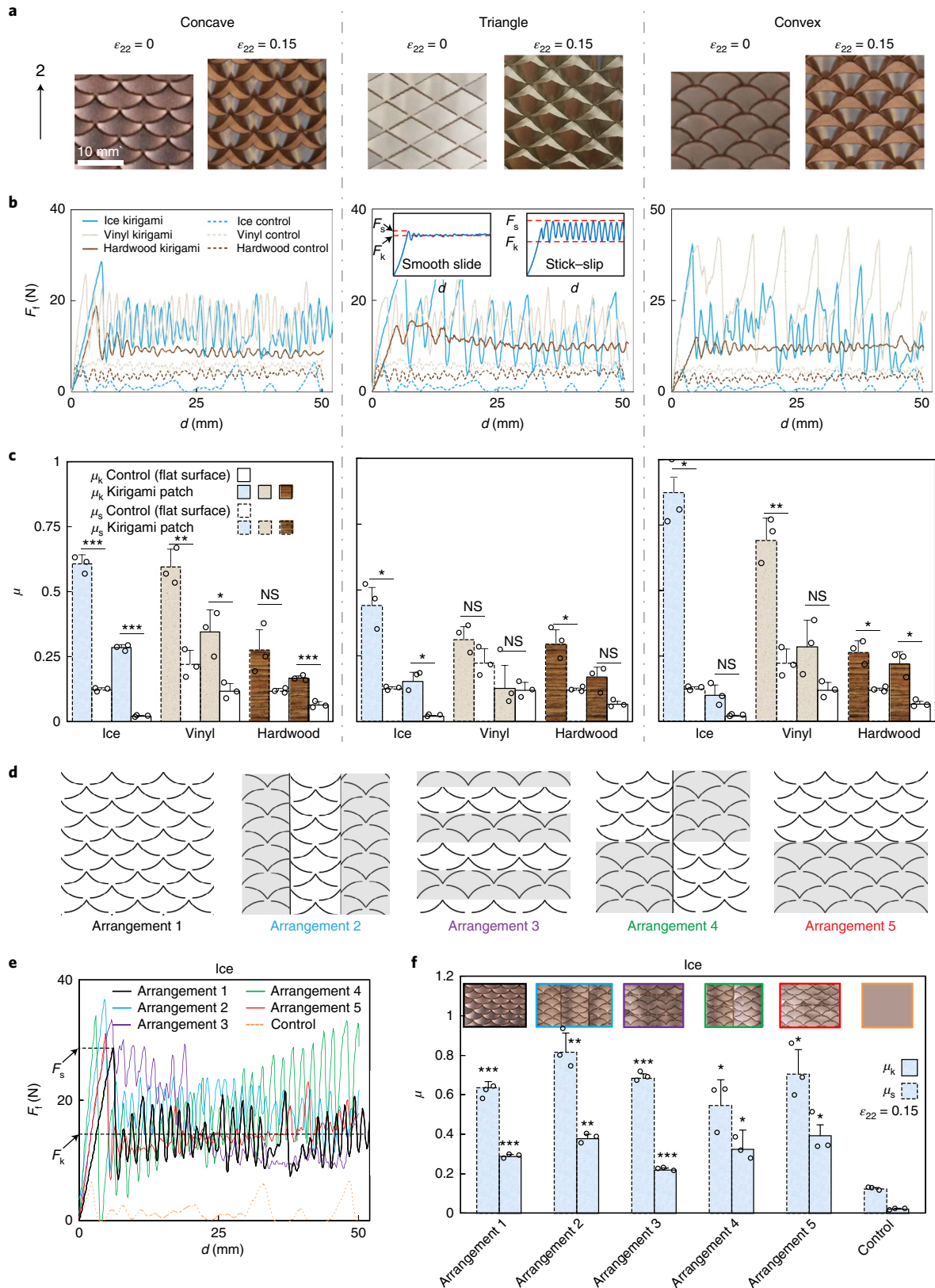
In vivo human force-plate measurements of the friction with the kirigami shoe grips. We conducted human-gait experiments using a force plate to further support the capacity of the kirigami patches to modulate friction during walking. Three human study participants wore a kirigami patch on the soles of their shoes and walked across a force plate covered with a 25.4-mm-thick layer of ice. Three orthogonal ground reaction forces exerted on the surface— F_x , F_y and F_z —were concurrently recorded (illustrated in Fig. 4a; see the Gait analysis section of Methods). The plot in Fig. 4a shows a typical gait response of walking over the first half of a gait cycle (that is, stance phase that includes the heel strike, support and toe-off stages) in the x direction. The response is characterized by a peak normal force in the z direction, an F_n equal to the weight of the study participant and a small peak friction force in the x direction during the weight-acceptance stage (that is, braking force), followed by a peak friction force in the negative x direction in the toe-off stage (that is, propulsion force denoted by F_s)^{42,43}. As expected, the force signal in the y direction was approximately zero and negligible. Note that the kirigami shoe grips were designed to operate during the toe-off

Fig. 3 | Friction enhancement of the kirigami shoe grips with various spike shapes and arrangements. **a**, Experimental images showing the configurations of the fabricated steel kirigami patches ($\gamma = 30^\circ$ and $\delta/l = 0.15$) with concave (left), triangular (middle) and convex (right) shapes at $\epsilon_{22} = 0$ and 0.15 (the 2 direction is shown). **b**, Measured friction force of the kirigami patches with different spike shapes as well as flat control patches on ice, vinyl and hardwood surfaces. Insets (middle), typical observed friction responses including smooth slide (left) and stick–slip (right). **c**, Experimentally determined static and dynamic coefficients of friction between the kirigami patches (pre-stretched at $\epsilon_{22} = 0.15$) with concave-, triangle- and convex-shaped spikes as well as flat control patches and ice, vinyl and hardwood surfaces. **d**, Schematics of kirigami patches with different spikes arrangements: arrangement 1, unidirectional; arrangement 2, three-column; arrangement 3, alternating rows; arrangement 4, chequered; and arrangement 5, mirror. **e**, Friction force versus the displacement response of the concave kirigami patches with different spike arrangements as well as flat control surfaces sliding on ice. **f**, Effect of different spike arrangements on the μ_s and μ_k values. Insets, different arrangements of the fabricated grips. Data are reported as the mean \pm s.d. of $n = 3$ measurements for each group. Two-sample Student’s t -tests were used to determine significance. * $P < 0.05$, ** $P < 0.01$, *** $P < 0.001$; NS, not significant (kirigami patch versus flat control surface for both μ_s and μ_k); d , displacement. Precise P values are provided in Supplementary Table 1.

stage, where the bending of the shoes triggers the kirigami spikes to buckle out and engage with the walking surfaces to increase friction.

The variation of the reaction forces in the x and z directions for study participant 1 wearing a kirigami shoe grip (arrangement 1), a control flat sheet as well as sneakers with grip and felt soles are

presented in Fig. 4b. The weight of the participant was $F_n \cong 750\text{ N}$, which was recorded almost identically in all of the tests. However, the peak friction force (F_s) had the highest value for the kirigami and then decreased for the sneakers and flat sheet, a signature of stronger friction enhancement of the kirigami shoe grip.



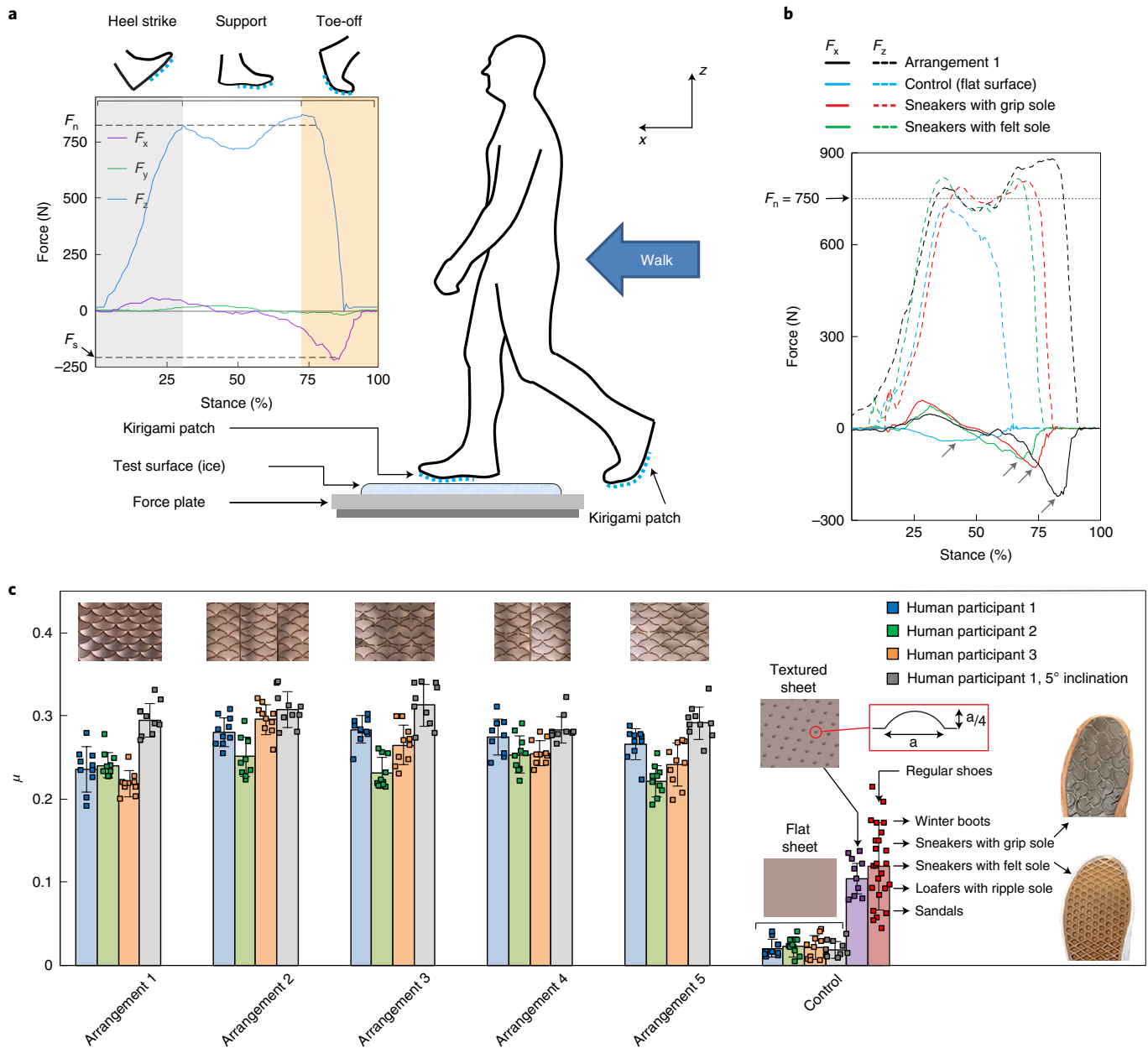


Fig. 4 | Kirigami shoe grip-induced changes in utilized friction coefficient on an ice surface. **a**, Illustration of the experimental set-up used to measure the forces exerted on the ice walking surface over the stance phase, which includes the heel strike (weight acceptance), support (foot flat) and toe-off (propulsion). Ground reaction forces in both the x (friction force) and z directions (human weight) were collected concurrently as the participants walked on the force plate covered with ice. Peak normal force in the z direction (F_n) and a peak friction force in the negative x direction (F_s) are shown. Data are plotted as the mean for $n=10$ measurements. **b**, Example of the reaction forces, F_x and F_z , recorded over a half gait cycle for study participant 1 wearing a kirigami grip (arrangement 1), control flat surface, sneakers with grip soles and sneakers with felt soles. The arrows point to the peak of propulsion reaction forces in the x direction (F_s). Data are plotted as the mean of $n=10$ measurements. **c**, Reported utilized coefficient of friction values for three study participants. The experiments were carried out while the participants were wearing the steel kirigami patches with different spike arrangements, the flat and textured control surfaces (shown in the insets) as well as various commercial shoes for comparison. The textured controls consisted of an embossed pattern in the form of a square array of dimples raised against the surface ($a=1$ mm). Images of the sneakers with grip and felt soles are shown (right). Data are reported as the mean \pm s.d. of $n=10$ measurements for each group.

Note that the gait experiment represents a much more complex and dynamic system (unlike the quasi-static experiments of Figs. 3 and 4) and as such, the μ values were interpreted as an effective measure of slip resistance when walking rather than a widely applicable property of two surfaces. We defined the utilized μ by normalizing the friction force with respect to the normal force, $\mu = F_s/F_n$. Five steel kirigami grips with different arrangements

were evaluated in addition to a control flat sheet of the base material (Fig. 4c). Furthermore, experiments using an ice surface (that is, an unmelted dry surface) at an inclination of 5° mounted on the force plate were conducted to inform the utilized μ in this setting (see Supplementary Information and Supplementary Fig. 7). In addition, gait evaluation was performed with a variety of commercial footwear—including winter boots, sneakers, loafers and

sandals—with various tread groove patterns designed to increase friction and provide a good grip to the wearer when walking in the shoes (see the inset in Fig. 4c). Notably, all three study participants exhibited average utilized friction coefficients in the range of $0.22 < \bar{\mu} < 0.30$ on flat ice for all of the spike arrangements, which is on average ten times more than that of the flat steel controls ($\bar{\mu} = 0.02$) and twice more than the textured steel controls ($\bar{\mu} = 0.10$; Fig. 4c, purple column) and commercial shoes ($\bar{\mu} = 0.12$; Fig. 4c, red column). The textured controls had the same thickness (0.051 mm) as the flat controls and kirigami patches (see the Fabrication of the kirigami patches section of Methods). The grey columns are the experimental data recorded using the inclined surface, which represents the utilized μ for study participant 1 wearing steel kirigami patches with the various arrangements of spikes on the soles of his shoes. The data showed an increase in shear forces for the inclined surface, which resulted in a growth of 10 to 20% in utilized friction coefficients with respect to the flat surfaces. These values were relatively consistent among all study participants, which provides support for the ice-gripping capacity of kirigami shoe grips through dynamic friction modulation.

Discussion

In summary, in view of the public health importance of reducing falls, we have harnessed kirigami-based metasurfaces to mitigate slipping and falling. We demonstrate that we are able to actively enhance the frictional properties between the soles of shoes and the walking/working surfaces by attaching stretchable lightweight steel kirigami patches to the shoe soles. In this work, we have introduced several key elements including: (1) the application of changes to the curvature of the soles of shoes during commercial walking to dynamically actuate the kirigami shoe grips (that is, without using any external source of energy) and (2) reversible frequent shape transformation from flat surfaces (low friction) to 3D surfaces with popped-up spikes (high friction), which enables us to tune friction dynamically (that is, no need to remove the kirigami shoe grips). We present a systematic study by combining finite-element simulations and experimental methods to investigate the effect of kirigami mesostructure (geometry, shape and arrangement of spikes) on the frictional properties between the kirigami shoe grips and walked-on icy surfaces.

Notably, our proposed kirigami shoe grips are capable of enhancing lateral frictional properties that enable a reduction in the risk of slips and falls transversally to the direction of movement (that is, biaxial friction enhancement). We observed that our symmetric kirigami pattern supports lateral friction force of a magnitude that is comparable to and even slightly larger than axial friction. Moreover, the introduction of asymmetry can further increase the lateral friction while axial friction remains in the same range (see the Kirigami shoe grips with biaxial friction control section of the Supplementary Information and Supplementary Fig. 8). This simple demonstration confirms that buckling-induced kirigami offer promising future directions and can be used to tune the frictional properties of patterned surfaces. This design can be expanded in further studies by the introducing curvilinear grids to enable a more pronounced change in the orientation of the spikes in lateral directions.

The typical walk consists of a repeated gait cycle that contains two phases: the first half cycle (stance phase), which can be divided into three stages—heel strike (weight acceptance), support (foot flat) and toe-off (propulsion)—and the second half cycle (swing phase), which includes leg lift and forward motion. The kirigami metasurfaces were designed to operate during the propulsion stage, where bending of the shoes induces stretching strain along the soles to activate the kirigami and generates higher friction forces in the forefoot. However, slipping during weight acceptance after heel contact (approximately 0–20% stance phase) is more hazardous compared with slipping during push-off. During the acceptance

phase (from heel contact to foot flat), the shoes are not substantially bent and the effect of increasing friction due to deformation of the kirigami metasurfaces may not be achieved. This is thus a limitation of this study and the potential area of future slip resistance research. However, the finite residual deformation (that is, slight localized plastic strains at the hinges) caused by deformation of the patches results in a surface that is not fully smooth at rest position and can be beneficial to increase the friction of unactuated patches over the foot-flat and toe-off stages (see the Effect of material behaviour on the response of kirigami shoe grips section of the Supplementary Information). The current kirigami grips cover only the top half of the sole. Therefore, the braking forces—generated from the interaction between the heel region of the shoe sole and ice in the weight-acceptance phase of gait—cannot be controlled and may vary for shoes made of various materials and sole groove patterns. Moreover, the attached kirigami grips may change the gait of the study participants and affect the braking forces. Therefore, we can make outsoles that cover the entire sole and consist of two portions to achieve further friction improvement over all of the stages of stance: (1) a top portion consisting of the kirigami pattern made of textured sheets to increase the friction in the push-off stage and (2) a bottom portion (heel region) made of dimpled or tread groove patterns (no kirigami pattern) to generate higher braking forces and increase friction in the weight-acceptance phase and finally reduce the risk of slip^{44–46}.

The proposed approach could be beneficial to reduce the risk of slip and fall for other slippery surfaces, including oily or wet hardwood floors and vinyl. The tribological mechanisms behind the kirigami patches could be further assessed with more detailed wear studies (for example, estimating wear volume through scratch depth in test surfaces and measuring the wear life) and in situ monitoring of the kirigami during tests to assess the degree of tip flattening and possibly ploughing. Stainless steel prototypes were employed to demonstrate the capacity of kirigami surfaces for dynamic modulation of friction. Future developments will include further evaluation of other materials, including composites, for field application. For example, they could be designed as a bilayer composite: a body made of a high-stiffness elastomer with microfeatures (for example, dimple and groove) and steel-reinforced spiked tips. An elastic body with grooves provides friction in the range of commercially available winter shoes or anti-slip solutions^{47,48}, and kirigami spikes provide extra friction enhancement through dynamic orienting. This can improve the lifetime of steel shoe grips under cycling loads (see the Experimental fatigue testing of the kirigami shoe grips section of the Supplementary Information and Supplementary Fig. 9). Future successful translation of these technologies will involve further human dynamic evaluation across all of the stages of stance^{49–51} and ambulation in ice-containing environments, including inclined surfaces^{9,52}. We envision morphable kirigami patches could be customized to the shape of the specific shoe soles of an individual by introducing a functional gradient in the size and shape of the spikes to provide the required friction force during daily activities.

Methods

Numerical simulations. The simulations were carried out using the commercial Finite Element package ABAQUS 2019 (SIMULIA). The Abaqus/Standard solver was employed for all simulations. In all of our analyses we discretized the sheets using four-node general-purpose shell elements with reduced integration and hourglass control (S4R Abaqus element type) and, guided by our experiments, modelled the cuts as elongated rectangular voids with a width of 0.1 mm. As plasticity has little effect on the observed phenomena (see the Effect of material behaviour on the response of kirigami shoe grips section of the Supplementary Information and Supplementary Fig. 10), the material behaviour of the steel sheets was captured using a linear elastic material model with an elastic $E = 193$ GPa and a Poisson's ratio, $\nu = 0.27$. To reduce the computational cost and ensure the response of the system was not dominated by boundary effects, we conducted analyses on unit cells subjected to periodic boundary conditions applied on opposite edges. Note that, in the finite size structures, the response is slightly affected by the effect

of the boundaries, and the morphology and characteristics of the emerging 3D pop-ups (for example, the relation between θ and the applied strain) are found to be unaltered (see the Stress-strain response of finite size kirigami under uniaxial tension section of the Supplementary Information and Supplementary Fig. 11). Two sets of analyses were performed, as detailed below.

Deformation of kirigami patches under uniaxial in-plane tensile strain. The uniaxial response of the kirigami structures was simulated in two steps: a linear perturbation analysis (*BUCKLE module in Abaqus) was used to identify the critical buckling mode and the nonlinear post-buckling response of the system was simulated by introducing a small imperfection (~ 0.005 of l) in the form of the critical mode into the initial geometry and conducting static analysis (*STATIC module in Abaqus).

Examination of the normal stiffness of the spikes. Following uniaxial tensile simulation of kirigami patches, the normal stiffness of buckled spikes was examined by subsequent compression of pre-stretched patches using a rigid plate while the displacement of the four corners of the unit cells were constrained in the normal direction. The plate was discretized using rigid shell elements and initially positioned slightly above the tip of the spikes, which were calculated from previous uniaxial tensile simulations. We performed dynamic implicit analysis (*DYNAMIC module in Abaqus) by lowering the plate until it pushed the spikes down by 0.25 mm. A simplified contact law (general contact-type interaction) was assigned to the model with a hard contact for normal behaviour and a frictionless tangential behaviour. The reaction force of the plate was recorded as a function of the applied displacement in the normal direction (Supplementary Fig. 12). Finally, the normal stiffness was given by calculating the initial slope of the force-displacement curve.

The ABAQUS scripts used for the above-mentioned analyses are available in Supplementary Information.

Fabrication of the kirigami patches. The metal kirigami patches were fabricated from 0.051-mm-thick 301 stainless steel shim stock (Rockwell hardness C32, Trinity Brand Industries, McMaster-Carr part no. 2316K11) and laser-cut using a Kern MICRO equipped with a 150 W laser. The dimension of the kirigami patches is 11 × 7 cm with 160 stretchable spikes, as shown in Supplementary Fig. 1a. The spikes were fabricated as different shapes, including concave, triangular and convex (Supplementary Fig. 1b). The fabricated kirigami patches in the undeformed ($\epsilon_{22} = 0$) and stretched ($\epsilon_{22} = 0.2$) configurations with various spike shapes and arrangements, including unidirectional, mirror, alternating rows, three-column and chequered, are shown in Supplementary Figs. 3 and 5. Both the flat and textured control patches were made of the same 301 stainless steel sheets with a thickness of 0.051 mm, Rockwell hardness C32 and a dimension of 11 × 7 cm. The textured controls were manufactured using a custom-made embossing hammer to create an embossed pattern consisting of a square array of dimples with a periodicity length of 5 mm (see the inset in Fig. 4c), which was raised against the surface of the flat sheet ($a = 1$ mm).

Friction testing. Friction testing was carried out using a custom attachment designed in-house for an Instron 5942 series universal testing system with a 500 N load cell, as shown in Supplementary Fig. 4. The attachment consists of a weighted sled, a table on which the sled slides and an M4 eyebolt that attaches to the crosshead of the testing machine and pulls the sled at a constant velocity of 10 mm s⁻¹ via a cotton twine string. The table is 600 mm long and 150 mm wide and made from a 6.35-mm-thick acrylic sheet. It has four 6-mm holes, which allow it to be screwed onto the base of the testing machine and a screw-mounted pulley (McMaster-Carr, part no. 3071T7) for the string. In addition, the table has two M6 tapped holes for 300-mm-long threaded rods (McMaster-Carr, part no. 93325A418) that support the weight of the table extending off the base. The sled is 165 mm long and 97 mm wide and is made from two 6.35 mm acrylic sheets stacked and held together by M4 screws. The top sheet functions as a barrier to prevent the weight from sliding off the top of the sled. Finally, it has an M4 eyebolt screwed to the front for the string, which is tied on both ends using a bowline knot.

To study the effects of spike shape and arrangement on the friction response of the patches, three shapes (concave, triangular and convex) with five arrangements (unidirectional, mirror, alternating rows, three-column and chequered) were each tested—a total of 15 different patches and one control patch (that is, flat sheet of stainless steel). Three different surfaces were tested: hardwood (Armstrong Flooring, item no. FP735WEAS502C14), vinyl (Armstrong Flooring, item no. FP84660159) and ice, which was made in-house by freezing water in a 34.3 × 24.4 × 7.0 cm aluminium tray overnight in a -20 °C freezer.

The patches were clamped to the sled to strain them to approximately 15% and a 5 kg weight was placed on top. The sled was pulled at a constant velocity of 10 mm s⁻¹ until it reached the end of the surface, resulting in a plot of (friction) force against extension. This was repeated five times per patch.

Gait analysis. Force-plate tests were carried out using an AMTI AccuGait Optimized force plate connected to a personal computer running the NetForce data acquisition software. Three healthy adults (two men and one woman; age, 24.6 ± 5.2 yr; mass, 75.0 ± 14.7 kg; height, 172 ± 12 cm; US shoe size,

9.3 ± 1.7; mean ± s.d.) participated in the study. The study was approved by the Massachusetts Institute of Technology Committee on the Use of Humans as Experimental Subjects (MIT COUHES) and carried out according to only the approved methods. The nature of the study, including its minimal risks, were explained to the participants, who then provided written consent to participate in the study. The participants were provided with a safety helmet, knee and elbow pads as well as access to a hand rail.

One surface, ice, and different metal patches were tested: concave-shaped spikes with five arrangements (unidirectional, three-column, alternating rows, chequered and mirror). Seven controls were tested: a flat steel sheet attached to the shoe sole (that is, no kirigami pattern), a dimple-textured steel sheet attached to the shoe sole and five commercial shoes (no patch)—winter boots, sneakers with grip soles, sneakers with felt soles, loafers with ripper soles and sandals. The ice surface was mounted on top of the 51 × 51 cm force plate. The ice was at -20 °C (unmelted dry surface from the freezer) at the beginning of the test, which provided ample time for the participants to perform the test before the ice started to melt. In cases where the ice was visibly scratched or started melting between tests, the ice was replaced before continuing with the tests, as multiple ice blocks were frozen and prepared for the experiment (variation of ice surface temperature shown in Supplementary Fig. 13). Each patch was attached to the shoe on the dominant foot of the participants by fixing both ends using duct tape to cover the top half of the sole. The participants then walked forward one step and stepped on the force plate ten times per patch. The step length and speed were not regulated. Each repeat resulted in a plot of three orthogonal forces and moments (in the x , y and z directions), of which only the directions corresponding to the normal (human weight) and friction forces were used, as shown in Fig. 4a.

Reporting Summary. Further information on research design is available in the Nature Research Reporting Summary linked to this article.

Data availability

The main data supporting the results of this study are available within the paper and its Supplementary Information. All of the data generated in this study, including the source data and the data used to make the figures, are available from figshare with the identifier <https://doi.org/10.6084/m9.figshare.12207992>.

Code availability

The ABAQUS scripts used for the numerical analyses are available as Supplementary Information.

Received: 18 July 2019; Accepted: 29 April 2020;

Published online: 01 June 2020

References

- Injury Facts. *National Safety Council* <https://injuryfacts.nsc.org/> (2017).
- Li, K., Courtney, T. & Huang, Y. Slipping and falling experience and perception of floor slipperiness: a field survey in 10 fast-food restaurants in Taiwan. *Prof. Saf.* **51**, 34–38 (2006).
- Morrison, R., Chassin, M. & Siu, A. The medical consultant's role in caring for patients with hip fracture. *Ann. Intern. Med.* **128**, 1010–1020 (1998).
- Wolinsky, F. D., Fitzgerald, J. F. & Stump, T. E. The effect of HIP fracture on mortality, hospitalization, and functional status: a prospective study. *Am. J. Public Health* **87**, 398–403 (1997).
- Panula, J. et al. Mortality and cause of death in hip fracture patients aged 65 or older—a population-based study. *BMC Musculoskelet. Disord.* **12**, 105 (2011).
- LeBlanc, E. S. et al. Hip fracture and increased short-term but not long-term mortality in healthy older women. *Arch. Intern. Med.* **171**, 1831–1837 (2011).
- Tinetti, M. E. et al. A multifactorial intervention to reduce the risk of falling among elderly people living in the community. *N. Engl. J. Med.* **331**, 821–827 (1994).
- Englander, F., Hodson, T. & Terregrossa, R. Economic dimensions of slip and fall injuries. *J. Forensic Sci.* **41**, 733–746 (1996).
- Hsu, J. et al. Slip resistance of winter footwear on snow and ice measured using maximum achievable incline. *Ergonomics* **59**, 717–728 (2016).
- Stevens, J. A., Corso, P. S., Finkelstein, E. A. & Miller, T. R. The costs of fatal and non-fatal falls among older adults. *Inj. Prev.* **12**, 290–295 (2006).
- Bureau of Labor Statistics, US Department of Labor. 42,480 work injuries involved ice, sleet, or snow in 2014. *The Economics Daily* <https://www.bls.gov/opub/ted/2016/42480-work-injuries-involved-ice-sleet-or-snow-in-2014.htm> (2016).
- Chang, W. R., Leclercq, S., Lockhart, T. E. & Haslam, R. State of science: occupational slips, trips and falls on the same level. *Ergonomics* **59**, 861–883 (2016).
- Hanson, J. P., Redfern, M. S. & Mazumdar, M. Predicting slips and falls considering required and available friction. *Ergonomics* **42**, 1619–1633 (1999).
- Gao, C. & Abeyssekera, J. A systems perspective of slip and fall accidents on icy and snowy surfaces. *Ergonomics* **47**, 573–598 (2004).

15. Gao, C., Holmér, I. & Abeyskera, J. Slips and falls in a cold climate: underfoot surface, footwear design and worker preferences for preventive measures. *Appl. Ergon.* **39**, 385–391 (2008).
16. Bruce, M., Jones, C. & Manning, D. P. Slip-resistance on icy surfaces of shoes, crampons and chains—a new machine. *J. Occup. Accid.* **7**, 273–283 (1986).
17. Gard, G. & Berggård, G. Assessment of anti-slip devices from healthy individuals in different ages walking on slippery surfaces. *Appl. Ergon.* **37**, 177–186 (2006).
18. Berggård, G. & Johansson, C. Pedestrians in wintertime—effects of using anti-slip devices. *Accid. Anal. Prev.* **42**, 1199–1204 (2010).
19. Gao, C., Abeyskera, J., Hirvonen, M. & Grönqvist, R. Slip resistant properties of footwear on ice. *Ergonomics* **47**, 710–716 (2004).
20. Menant, J. C., Steele, J. R., Menz, H. B., Munro, B. J. & Lord, S. R. Optimizing footwear for older people at risk of falls. *J. Rehabil. Res. Dev.* **45**, 1167–1181 (2008).
21. Blees, M. K. et al. Graphene kirigami. *Nature* **524**, 204–207 (2015).
22. Rafsanjani, A. & Bertoldi, K. Buckling-induced kirigami. *Phys. Rev. Lett.* **118**, 084301 (2017).
23. Tang, Y. et al. Programmable kiri-kirigami metamaterials. *Adv. Mater.* **29**, 1604262 (2017).
24. Zhang, Y. et al. A mechanically driven form of kirigami as a route to 3D mesostructures in micro/nanomembranes. *Proc. Natl Acad. Sci. USA* **112**, 11757–11764 (2015).
25. Liu, Z. et al. Nano-kirigami with giant optical chirality. *Sci. Adv.* **4**, eaat4436 (2018).
26. Wu, C., Wang, X., Lin, L., Guo, H. & Wang, Z. L. Paper-based triboelectric nanogenerators made of stretchable interlocking kirigami patterns. *ACS Nano* **10**, 4652–4659 (2016).
27. Jang, N. S. et al. Simple approach to high-performance stretchable heaters based on kirigami patterning of conductive paper for wearable thermotherapy applications. *ACS Appl. Mater. Interfaces* **9**, 19612–19621 (2017).
28. Rafsanjani, A., Zhang, Y., Liu, B., Rubinstein, S. M. & Bertoldi, K. Kirigami skins make a simple soft actuator crawl. *Sci. Robot.* **3**, eaar7555 (2018).
29. Dias, M. A. et al. Kirigami actuators. *Soft Matter* **13**, 9087–9092 (2017).
30. Zheng, W. et al. Kirigami-inspired highly stretchable nanoscale devices using multidimensional deformation of monolayer MoS₂. *Chem. Mater.* **30**, 6063–6070 (2018).
31. Morikawa, Y. et al. Ultrastretchable kirigami bioprobes. *Adv. Healthc. Mater.* **7**, 1701100 (2018).
32. Shyu, T. C. et al. A kirigami approach to engineering elasticity in nanocomposites through patterned defects. *Nat. Mater.* **14**, 785–789 (2015).
33. Ma, R., Wu, C., Wang, Z. L. & Tsukruk, V. V. Pop-up conducting large-area biographene kirigami. *ACS Nano* **12**, 9714–9720 (2018).
34. Song, Z. et al. Kirigami-based stretchable lithium-ion batteries. *Sci. Rep.* **5**, 10988 (2015).
35. Wilson, A. M. et al. Locomotion dynamics of hunting in wild cheetahs. *Nature* **498**, 185–189 (2013).
36. Skutch, A. F. *Helpers At Birds' Nests: Cooperative Breeding and Related Behaviour* (Univ. of Iowa Press, 1999).
37. Marvi, H. & Hu, D. L. Friction enhancement in concertina locomotion of snakes. *J. R. Soc. Interface* **9**, 3067–3080 (2012).
38. Guo, Z. V. & Mahadevan, L. Limbless undulatory propulsion on land. *Proc. Natl Acad. Sci. USA* **105**, 3179–3184 (2008).
39. Suh, N. P. & Sin, H.-C. The genesis of friction. *Wear* **69**, 91–114 (1981).
40. Lee, D. W., Banquy, X. & Israelachvili, J. N. Stick-slip friction and wear of articular joints. *Proc. Natl Acad. Sci. USA* **110**, 567–574 (2013).
41. Das, S. et al. Stick-slip friction of gecko-mimetic flaps on smooth and rough surfaces. *J. R. Soc. Interface* **12**, 20141346 (2015).
42. Giakas, G. & Baltzopoulos, V. Time and frequency domain analysis of ground reaction forces during walking: an investigation of variability and symmetry. *Gait Posture* **5**, 189–197 (1997).
43. Lieberman, D. E. et al. Foot strike patterns and collision forces in habitually barefoot versus shod runners. *Nature* **463**, 531–535 (2010).
44. Li, K. W. et al. The effect of shoe sole tread groove depth on the friction coefficient with different tread groove widths, floors and contaminants. *Appl. Ergon.* **37**, 743–748 (2006).
45. Yamaguchi, T. & Hokkirigawa, K. Development of a high slip-resistant footwear outsole using a hybrid rubber surface pattern. *Ind. Health* **52**, 414–423 (2014).
46. Yamaguchi, T. et al. Efficacy of a rubber outsole with a hybrid surface pattern for preventing slips on icy surfaces. *Appl. Ergon.* **51**, 9–17 (2015).
47. Rizvi, R., Naguib, H., Fernie, G. & Dutta, T. High friction on ice provided by elastomeric fiber composites with textured surfaces. *Appl. Phys. Lett.* **106**, 111601 (2015).
48. Ion, A., Kovacs, R., Schneider, O., Lopez, P. & Baudisch, P. Metamaterial textures. In *Proc. CHI Conference on Human Factors in Computing Systems* 336 (Association for Computing Machinery, 2018).
49. Iraqi, A., Cham, R., Redfern, M. S., Vidic, N. S. & Beschoner, K. E. Kinematics and kinetics of the shoe during human slips. *J. Biomech.* **74**, 57–63 (2018).
50. McGorry, R. W., Chang, C. C. & DiDomenico, A. Rearward movement of the heel at heel strike. *Appl. Ergon.* **39**, 678–684 (2008).
51. Powers, C. M., Blanchette, M. G., Brault, J. R., Flynn, J. & Siegmund, G. P. Validation of walkway tribometers: establishing a reference standard. *J. Forensic Sci.* **55**, 366–370 (2010).
52. Hsu, J., Li, Y., Dutta, T. & Fernie, G. Assessing the performance of winter footwear using a new maximum achievable incline method. *Appl. Ergon.* **50**, 218–225 (2015).

Acknowledgements

We thank T. Hua, M. Cruz, N. Inverardi, X. Lu and V. Soares for their help with the experimental studies; S. Cotreau, C. Haynes and A. Wentworth for help with manufacturing the experimental specimens; and R. Langer for fruitful discussions. This work was funded in part by a start-up grant from the Department of Mechanical Engineering, MIT to G.T. K.B. acknowledges support from the National Science Foundation under grant nos. DMR-1420570 (Materials Research Science and Engineering Center) and EFRI C3 SoRo 1830896. A.R. acknowledges support from Swiss National Science Foundation grant no. P300P2-164648.

Author contributions

S.B., S.P., A.R., K.B. and G.T. conceived and designed the research. S.B., S.P. and A.R. designed the kirigami prototypes. S.B., S.P. and Y.S. performed the manufacturing, in vitro friction testing and human-gait force-plate measurements. A.R. performed the simulations. S.B., S.P., A.R., K.B. and G.T. discussed and analysed the results and wrote the manuscript. All authors reviewed the manuscript and provided active and valuable feedback.

Competing interests

A.R. and K.B. are inventors on a patent application (patent no. US2019/0232598A1) describing buckling-induced kirigami. S.B., S.P., A.R., K.B. and G.T. are co-inventors on a provisional patent application (no. 62913419) for the technology described. Complete details of all relationships for profit and not for profit for G.T. can be found at the following link: <https://www.dropbox.com/sh/szi7vnr4a2ajb56/AABs5N5i0q9AfT1IqIJAE-T5a?dl=0>. The remaining authors disclose no competing interests.

Additional information

Supplementary information is available for this paper at <https://doi.org/10.1038/s41551-020-0564-3>.

Correspondence and requests for materials should be addressed to K.B. or G.T.

Reprints and permissions information is available at www.nature.com/reprints.

Publisher's note Springer Nature remains neutral with regard to jurisdictional claims in published maps and institutional affiliations.

© The Author(s), under exclusive licence to Springer Nature Limited 2020

Reporting Summary

Nature Research wishes to improve the reproducibility of the work that we publish. This form provides structure for consistency and transparency in reporting. For further information on Nature Research policies, see [Authors & Referees](#) and the [Editorial Policy Checklist](#).

Statistics

For all statistical analyses, confirm that the following items are present in the figure legend, table legend, main text, or Methods section.

- | n/a | Confirmed |
|-------------------------------------|--|
| <input type="checkbox"/> | <input checked="" type="checkbox"/> The exact sample size (n) for each experimental group/condition, given as a discrete number and unit of measurement |
| <input type="checkbox"/> | <input checked="" type="checkbox"/> A statement on whether measurements were taken from distinct samples or whether the same sample was measured repeatedly |
| <input type="checkbox"/> | <input checked="" type="checkbox"/> The statistical test(s) used AND whether they are one- or two-sided
<i>Only common tests should be described solely by name; describe more complex techniques in the Methods section.</i> |
| <input checked="" type="checkbox"/> | <input type="checkbox"/> A description of all covariates tested |
| <input checked="" type="checkbox"/> | <input type="checkbox"/> A description of any assumptions or corrections, such as tests of normality and adjustment for multiple comparisons |
| <input type="checkbox"/> | <input checked="" type="checkbox"/> A full description of the statistical parameters including central tendency (e.g. means) or other basic estimates (e.g. regression coefficient) AND variation (e.g. standard deviation) or associated estimates of uncertainty (e.g. confidence intervals) |
| <input type="checkbox"/> | <input checked="" type="checkbox"/> For null hypothesis testing, the test statistic (e.g. F , t , r) with confidence intervals, effect sizes, degrees of freedom and P value noted
<i>Give P values as exact values whenever suitable.</i> |
| <input checked="" type="checkbox"/> | <input type="checkbox"/> For Bayesian analysis, information on the choice of priors and Markov chain Monte Carlo settings |
| <input checked="" type="checkbox"/> | <input type="checkbox"/> For hierarchical and complex designs, identification of the appropriate level for tests and full reporting of outcomes |
| <input checked="" type="checkbox"/> | <input type="checkbox"/> Estimates of effect sizes (e.g. Cohen's d , Pearson's r), indicating how they were calculated |

Our web collection on [statistics for biologists](#) contains articles on many of the points above.

Software and code

Policy information about [availability of computer code](#)

Data collection

Force-plate tests were carried out using an AMTI AccuGait Optimized force plate connected to a PC running the NetForce data acquisition software.

Data analysis

The simulations were carried out using the commercial Finite Element (FE) package ABAQUS 2019 (SIMULIA, Providence, RI).

For manuscripts utilizing custom algorithms or software that are central to the research but not yet described in published literature, software must be made available to editors/reviewers. We strongly encourage code deposition in a community repository (e.g. GitHub). See the Nature Research [guidelines for submitting code & software](#) for further information.

Data

Policy information about [availability of data](#)

All manuscripts must include a [data availability statement](#). This statement should provide the following information, where applicable:

- Accession codes, unique identifiers, or web links for publicly available datasets
- A list of figures that have associated raw data
- A description of any restrictions on data availability

The main data supporting the results in this study are available within the paper and its Supplementary Information. All data generated in this study, including source data and the data used to make the figures, are available from figshare with the identifier <https://doi.org/10.6084/m9.figshare.12207992>.

Field-specific reporting

Please select the one below that is the best fit for your research. If you are not sure, read the appropriate sections before making your selection.

Life sciences Behavioural & social sciences Ecological, evolutionary & environmental sciences

For a reference copy of the document with all sections, see [nature.com/documents/nr-reporting-summary-flat.pdf](https://www.nature.com/documents/nr-reporting-summary-flat.pdf)

Life sciences study design

All studies must disclose on these points even when the disclosure is negative.

Sample size	For the human studies, three subjects consented to the evaluation.
Data exclusions	No data were excluded.
Replication	For in vitro characterizations, each experiment was performed 3 times. The human force-plate friction measurements were performed 10 times
Randomization	Not applicable to this study.
Blinding	Not applicable to this study.

Reporting for specific materials, systems and methods

We require information from authors about some types of materials, experimental systems and methods used in many studies. Here, indicate whether each material, system or method listed is relevant to your study. If you are not sure if a list item applies to your research, read the appropriate section before selecting a response.

Materials & experimental systems

n/a	Involvement in the study
<input checked="" type="checkbox"/>	<input type="checkbox"/> Antibodies
<input checked="" type="checkbox"/>	<input type="checkbox"/> Eukaryotic cell lines
<input checked="" type="checkbox"/>	<input type="checkbox"/> Palaeontology
<input checked="" type="checkbox"/>	<input type="checkbox"/> Animals and other organisms
<input type="checkbox"/>	<input checked="" type="checkbox"/> Human research participants
<input checked="" type="checkbox"/>	<input type="checkbox"/> Clinical data

Methods

n/a	Involvement in the study
<input checked="" type="checkbox"/>	<input type="checkbox"/> ChIP-seq
<input checked="" type="checkbox"/>	<input type="checkbox"/> Flow cytometry
<input checked="" type="checkbox"/>	<input type="checkbox"/> MRI-based neuroimaging

Human research participants

Policy information about [studies involving human research participants](#)

Population characteristics	Three healthy adults (two men and one woman, age 24.6±5.2 years; mass 75.0±14.7 kg; height 172±12 cm; US shoe size 9.3±1.7; mean ± SD) participated in the study.
Recruitment	A poster advertisement at MIT was used for recruitment.
Ethics oversight	The study was approved by the Massachusetts Institute of Technology Committee on the Use of Humans as Experimental Subjects (MIT COUHES), and carried out according only to the approved methods.

Note that full information on the approval of the study protocol must also be provided in the manuscript.

In the format provided by the authors and unedited.

Bioinspired kirigami metasurfaces as assistive shoe grips

Sahab Babaee^{1,2,7}, Simo Pajovic^{1,2,3,7}, Ahmad Rafsanjani^{4,7} , Yichao Shi^{2,3}, Katia Bertoldi⁵   and Giovanni Traverso^{1,2,6}  

¹Department of Mechanical Engineering, Massachusetts Institute of Technology, Cambridge, MA, USA. ²Department of Chemical Engineering and Koch Institute for Integrative Cancer Research, Massachusetts Institute of Technology, Cambridge, MA, USA. ³Department of Mechanical and Industrial Engineering, University of Toronto, Toronto, Ontario, Canada. ⁴Department of Materials, ETH Zurich, Zurich, Switzerland. ⁵John A. Paulson School of Engineering and Applied Sciences, Harvard University, Cambridge, MA, USA. ⁶Division of Gastroenterology, Department of Medicine, Brigham and Women's Hospital, Harvard Medical School, Boston, MA, USA. ⁷These authors contributed equally: Sahab Babaee, Simo Pajovic, Ahmad Rafsanjani. e-mail: bertoldi@seas.harvard.edu; cgt20@mit.edu

Table of Contents

Supplementary Notes

Fig. S1. Fabricated steel kirigami shoe grips.

Fig. S2. Distribution of strains along a shoe sole over a half gait cycle.

Fig. S3. Fabricated kirigami shoe grips with different spike shapes.

Fig. S4. Friction testing set-up.

Fig. S5. Fabricated steel kirigami shoe grips with different spike arrangements.

Fig. S6. Friction enhancement of the concave kirigami shoe grips with various spike arrangements.

Fig. S7. Illustration of the force plate testing set-up on an inclined ice surface.

Fig. S8. Biaxial friction control using kirigami surfaces.

Fig. S9. Experimental fatigue tests.

Fig. S10. Effect of material behavior on the response of kirigami structures subjected to uniaxial tension.

Fig. S11. Stress-strain response of finite size kirigami under uniaxial tension.

Fig. S12. Evolution of normal stiffness of the kirigami surfaces.

Fig. S13: Variation of ice surface temperature during human force plate measurement of friction with kirigami shoe grips.

Table S1. Precise P values reported from the two-sample t tests used to determine the significance in Fig. 3.

Movie S1. Steel kirigami shoe grips attached to a shoe sole.

Movie S2. Finite element simulation of kirigami unit cell.

Supplementary Notes

Evaluation of utilized coefficient of friction on an inclined surface

We have conducted further experiments to evaluate utilized coefficient of friction using an inclined surface. The ice surface was mounted on top of the 51×51 cm force plate with an ascending inclined angle, $\theta = 5^\circ$ (Fig. S7). F_x and F_z are the ground reaction forces in x- and z-directions recorded by the force plate during walking over the half of a gait cycle. The utilized coefficient of friction (μ) was then calculated by:

$$\mu = \frac{F_t}{F_n} = \frac{F_x \cos\theta + F_z \sin\theta}{F_z \cos\theta - F_x \sin\theta}$$

, where F_t and F_n are the reaction forces in t - and n -directions. The detailed protocol of gait trials and instruction to the subject for walking on the inclined surface were the same as flat surfaces, described in the Methods section.

Kirigami shoe grips with biaxial friction control

Fig. S8A shows the design of two triangle kirigami structures with symmetric and asymmetric arrays of spikes. In the asymmetric design, the rows of tips of each spike are alternately shifted by the quarter of the unit cell's width to the right and left. We prototyped the kirigami out of 0.127 mm thick polyester plastic shim stock (Artus Corporation, NJ), and performed friction tests using the custom-built friction set-up (see fig. S4 and "Friction testing" in Methods). The kirigami were stretched $\epsilon_{22} = 0.15$ in 2-direction (Fig. S8B) that results in buckling out of the spikes, and then clamped to the sled with 5 kg weight on the top. The sled was pulled at a constant velocity of 10 mm/s in the 2-direction until reaching the end of the hardwood surface. Then, to evaluate the friction forces in the lateral direction, we repeated the same test by pulling the sled in the 1-direction. In Fig. S8C, we reported the friction forces (F_f) between kirigami (prestretched at $\epsilon_{22} = 0.15$) with symmetric (left plot) and asymmetric (right plot) arrays of spikes and a hardwood surface as a function of displacement. F_f^1 and F_f^2 are the recorded friction forces in the 1- and 2-directions, shown by dashed and solid lines, respectively. Each test was performed three times with the new kirigami, shown by different colors in Fig. S8C. Interestingly, the data demonstrates that not only both kirigami are capable of biaxial friction enhancement, but also the friction forces in the lateral direction (F_f^1) are higher than the forces in the axial direction (F_f^2). This lateral friction enhancement is even more pronounced for the asymmetric kirigami design.

Experimental fatigue testing of the kirigami shoe grips

We carried out fatigue testing to predict the life of steel shoe grips under cyclic tensile loads. An Instron 5942 series Universal Testing System with a 500 N load cell was used to apply cyclic uniaxial loading under strain-controlled conditions to the specimens (kirigami structures). A 2.5 mm thick ice block (300 ×120 mm) was mounted with the dry surface in a vertical orientation in contact with the kirigami surfaces such that the tips of the kirigami spikes

scratched the ice block while the top crosshead of the testing machine pulled or pushed the kirigami. All tests were conducted using a trapezoidal waveform with $\varepsilon_{Applied}^{max} = 0.15$, shown in Fig. S9. To determine the fatigue life, the specimen failure was defined at the point when a 50% drop in the maximum load (compared to the first cycle) or rupture is recorded. In Fig. S9, we reported the peak force in each cycle, F_{max} , versus the number of loading cycles, n , for the kirigami structures with concave, triangle, and convex spike shapes. We found that the concave kirigami prototypes fail at $n \sim 1700$ cycles, while the triangle and convex kirigami fail at $n \sim 1100$ and $n \sim 900$ cycles, respectively.

Effect of material behavior on the response of kirigami shoe grips

We examined the effect of plasticity and investigated the response of both elastic and elastoplastic kirigami structures under uniaxial tensile loads. We performed FE simulations by assuming an elastic-perfectly plastic material model (with yield stress $\sigma_y = 759$ MPa for 301 stainless steel) under cyclic loading (5 cycles), and compared the results to those obtained for purely elastic kirigami sheets. The results reported in Fig. S10 are for steel kirigami patches with concave, triangle, and convex spike shapes characterized by $\gamma = 30^\circ$, $\delta/l = 0.15$. Our finding suggests that while the effective stress-strain response of kirigami patches is affected by plasticity beyond out-of-plane buckling regime (Fig. S10A), the plastic strains localized in the hinges are moderate and the residual macroscopic strain is below 2% for all three patterns (Fig. S10B). From a practical point of view, this residual deformation can be beneficial since it potentially increases the friction of unactuated patches. Moreover, the effect of plasticity on tilting angle of kirigami sheets is negligible (Fig. S10C). Although the residual deformations caused by plasticity at the hinges are inevitable, the plastic deformation does not affect the morphology of the emerging 3D pop-ups, as their characteristics e.g. relation between tilting angle and applied strain are found to be unaltered.

Stress-strain response of finite size kirigami under uniaxial tension

We performed finite size simulations for kirigami structures with triangular cut pattern comprised of 16×2 , 16×4 , 16×6 , 16×8 units and compared the results with those obtained from periodic boundary conditions (PBC). For kirigami structures, three deformation regimes are identified: (i) initial linear regime, (ii) out of plane buckling and departure from linearity, and (iii) hardening due to stretching of the hinges. As shown in Fig. S11, the linear regime is similar for all the samples due to in-plane deformation. By increasing the number of unit cells, the critical strain at which the out-of-plane buckling initiates becomes closer to the response of PBC. On the other hand, increasing the number of horizontal unit cells results in constraining more units at the boundaries, which affects the hardening regime. Therefore, through the application of periodic boundary conditions, we avoid the dependency of the presented results on the choice of the number of units and save computational costs. We confirm that for real applications, the periodic boundary condition can be used as a guide while the results of finite size models should also be considered in the final prototypes.

Supplementary Figures

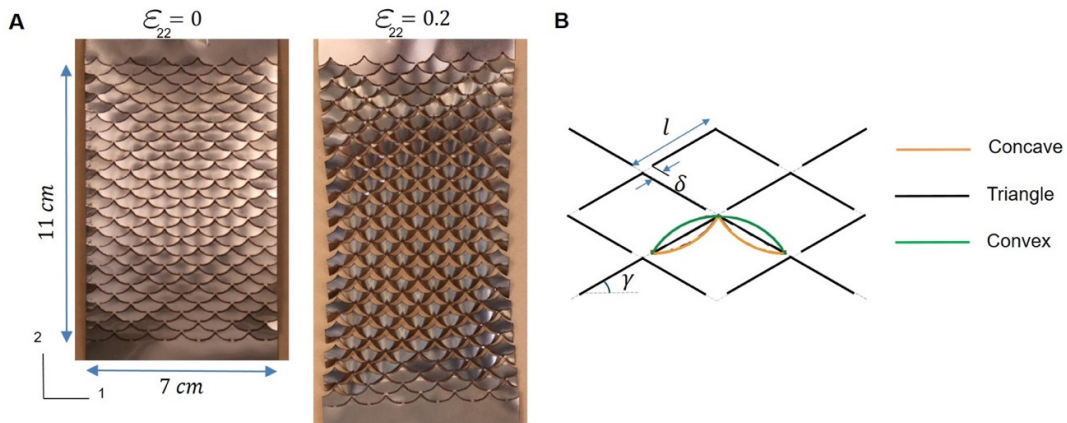


Figure S1: Fabricated steel kirigami shoe grips. (A) Undeformed ($\varepsilon_{22} = 0$) and stretched ($\varepsilon_{22} = 0.2$) configurations of the stainless steel kirigami patch made of a periodic array of concave-shaped spikes perforated in one direction. (B) The schematics of different spike shapes (in the middle) including concave (orange), triangle (black), and convex (green) with identical cut-angle ($\gamma = 30^\circ$) and hinge over cut-length ratio ($\delta/l = 0.15$).

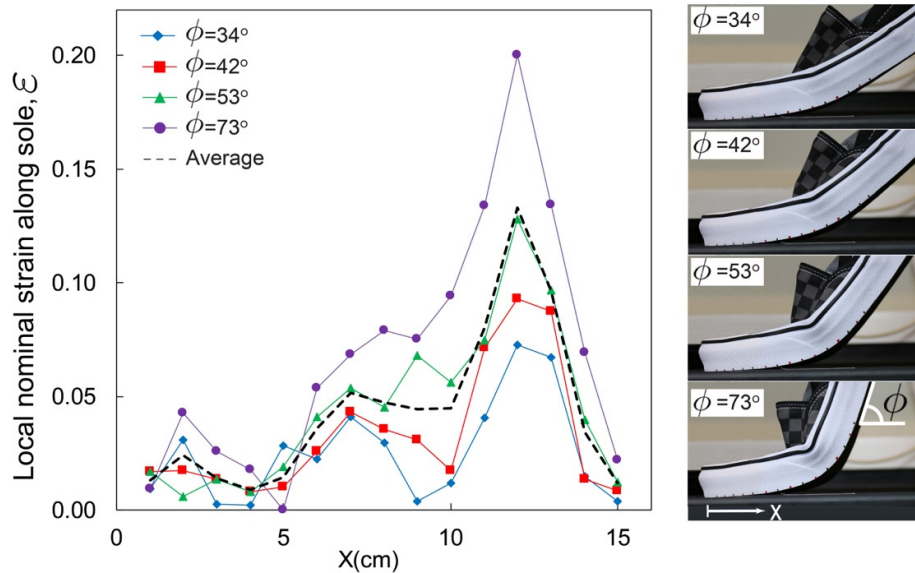


Figure S2: Distribution of strains along a shoe sole over a half gait cycle. The local strains, ε , were reported for different angles between the shoe sole and the walking surface ($\phi = 34^\circ$ (blue), 42° (red), 53° (green), and 73° (purple)) as a function of distance (x) from the shoe tip. The snapshots showing the shape of the shoe at the different angles are illustrated on the right.

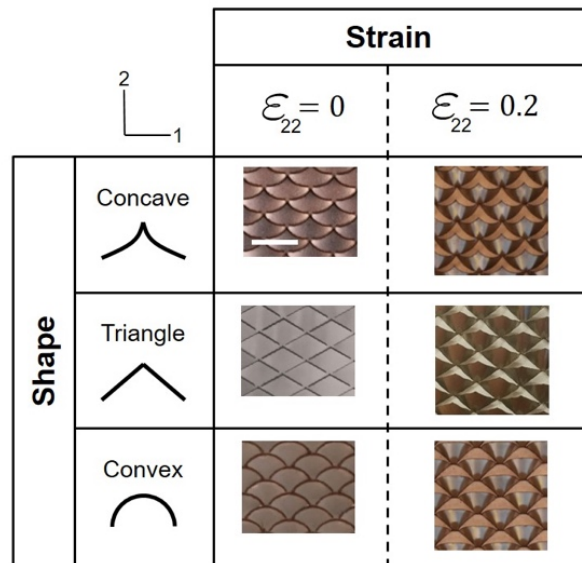


Figure S3: Fabricated kirigami shoe grips with different spike shapes. Undeformed ($\epsilon_{22}=0$) and stretched ($\epsilon_{22}=0.2$) configurations of the stainless steel kirigami patches with different spike shapes including concave, triangle, and convex that were considered for this study. Scale bar is 10 mm.

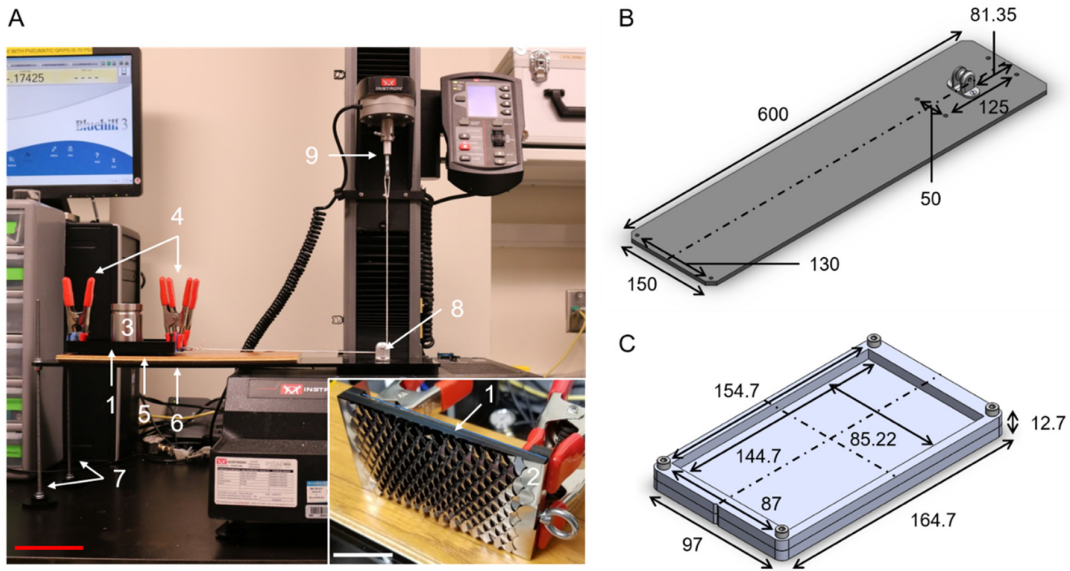


Figure S4: Friction testing set-up. (A) A universal testing machine (Instron 5942 series) with a 500 N load cell was used to evaluate the friction properties of the kirigami patches for various surfaces. The set-up (side view in the image) includes: (1) friction testing sled (bottom side shown in inset image) (2) kirigami patch, (3) weight, (4) clamps used to secure kirigami patch in the deformed state at 0.2 strain, (5) test surface (e.g., wood), (6) friction testing table, (7) M6 threaded rods used to support friction testing table, (8) low-friction pulley, and (9) hook attachment for crosshead to pull sled. Red scale bar is 100 mm; white scale bar in inset is 20 mm. The inset image is a bottom view of the friction testing sled with the kirigami patch attached. (1) and (2) are consistent with the outer image. The CAD model of the friction testing table (6) and sled without a kirigami patch (1) are illustrated in an isometric view in (B) and (C), respectively. All dimensions are in mm.

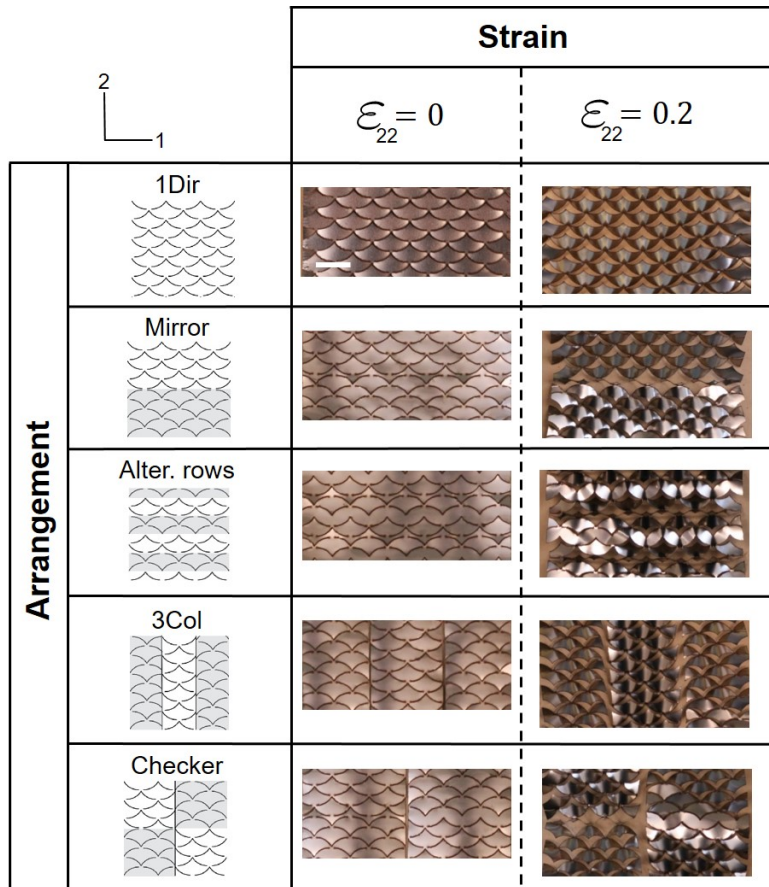


Figure S5: Fabricated steel kirigami shoe grips with different spike arrangements. Undeformed ($\epsilon_{22} = 0$) and stretched ($\epsilon_{22} = 0.2$) configurations of the stainless steel kirigami patches with different arrangements of spikes including Unidirectional (1Dir), Mirror, Alternating rows, 3-column, and Checker that were considered for this study. Scale bar is 10 mm.

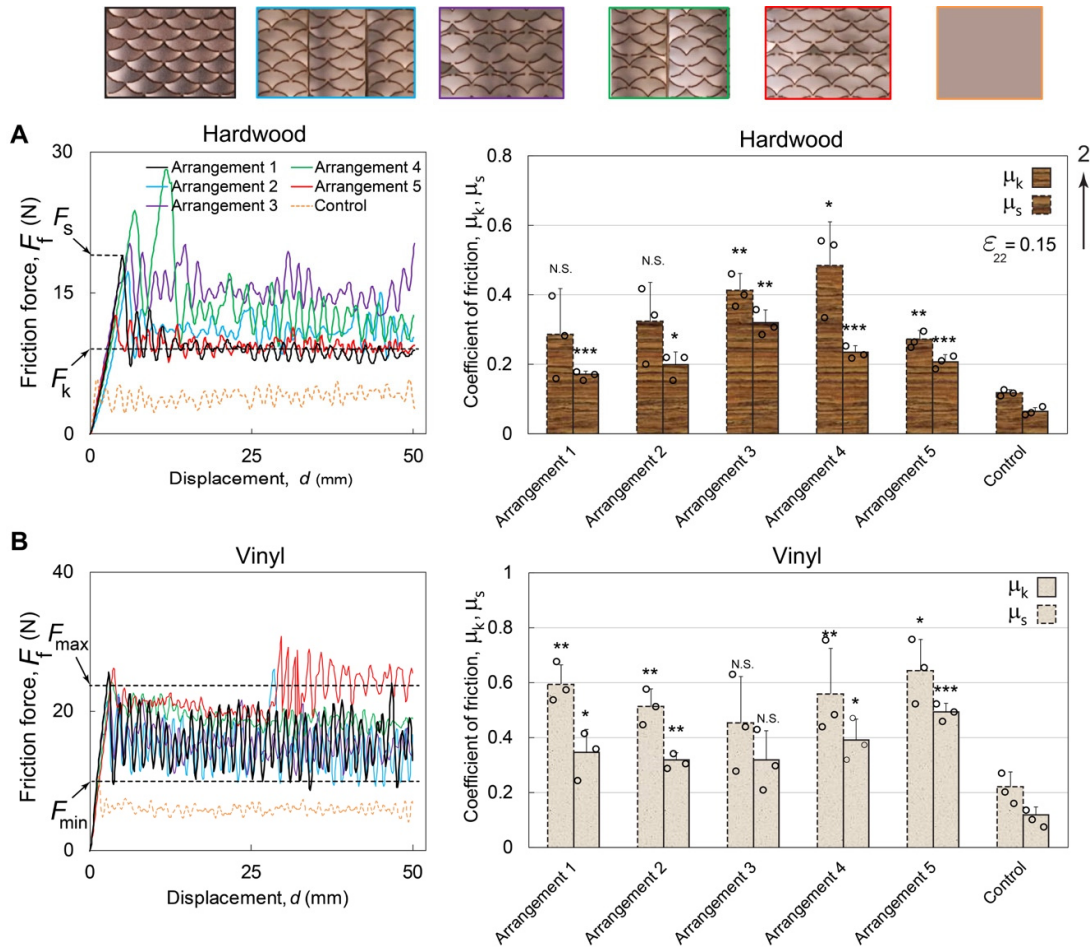


Fig S6. Friction enhancement of the concave kirigami shoe grips with various spike arrangements. Friction force (F_f) vs. displacement (d) response of the concave kirigami surfaces with different spike arrangements prestretched at $\epsilon_{22} = 0.15$ and control flat surfaces (orange), sliding on (A) hardwood, and (B) vinyl surfaces. F_s and F_k are the static and kinetic friction forces. Effect of different spike arrangements on static and dynamic friction coefficients (μ_s and μ_k) for kirigami surfaces prestretched at $\epsilon_{22} = 0.15$ are reported on the right. The different arrangements of the fabricated kirigami grips including arrangement 1 (Unidirectional in black), arrangement 2 (3-column in blue), arrangement 3 (Alternating rows in purple), arrangement 4 (Checker in green), and arrangement 5 (Mirror in red) are shown in the top. Interestingly, all the kirigami demonstrated enhanced frictional properties as compared to the control spikeless patch (orange dashed line), showing the smooth sliding for hardwood and stick-slip response for vinyl. The bar plots show considerable increases in μ_s (two- to three-fold) and μ_k (three- to four-fold) in average for all the arrangements with respect to the controls for both hardwood and vinyl. Data reported as mean \pm standard deviation for $n = 3$ measurements for each group. Two-sample t tests were used to determine the significance. * $P < 0.05$, ** $P < 0.01$, *** $P < 0.001$, and N.S. not significant (kirigami patch versus control flat surface for both μ_s and μ_k).

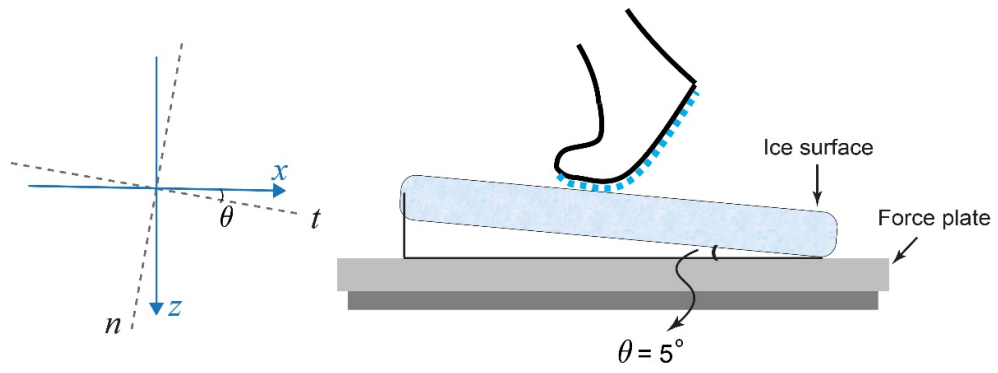


Fig S7. Illustration of force plate testing set-up on an inclined ice surface.

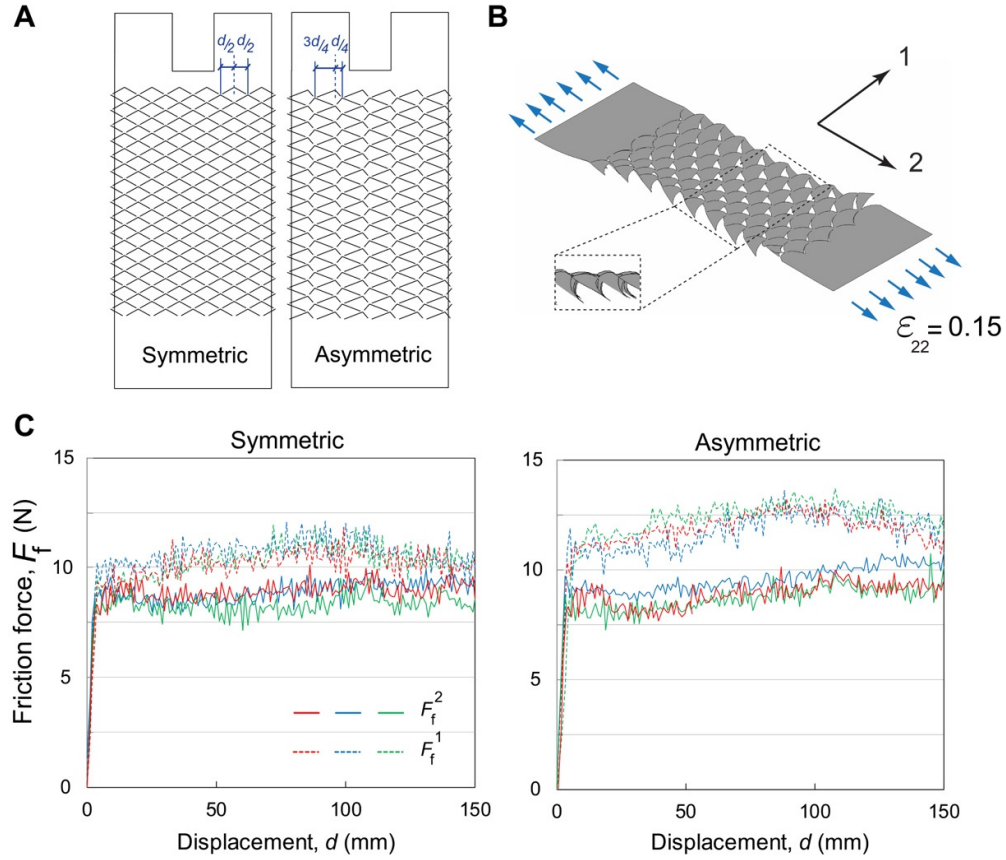


Fig. S8: Biaxial friction control using kirigami surfaces. (A) CAD models of triangle kirigami surfaces with symmetric and asymmetric arrays of spikes. d is the width of a unit cell. (B) The kirigami can be stretched $\epsilon_{22} = 0.15$ in 2-direction that results in out of plane buckling of the spikes. (C) Friction forces (F_f) between kirigami (prestretched at $\epsilon_{22} = 0.15$) with symmetric (left plot) and asymmetric (right plot) array of spikes and hardwood surface as a function of displacement. F_f^1 and F_f^2 are the recorded friction forces in 1- and 2-directions, shown by dashed and solid lines, respectively. Each test was performed three times shown by different colors.

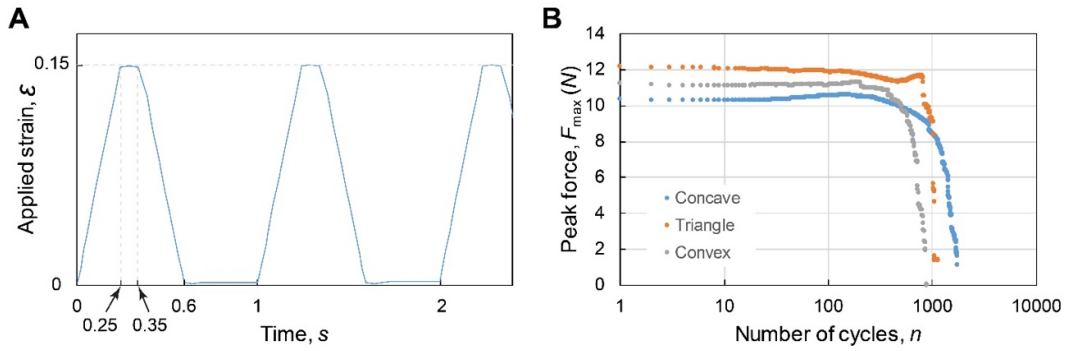


Fig. S9: Experimental fatigue tests. (A) Trapezoidal waveform used in the cyclic tests to control the applied strain. (B) Maximum recorded applied force, F_{max} , versus the number of loading cycles, n , for the kirigami structures with concave, triangle, and convex spike shapes.

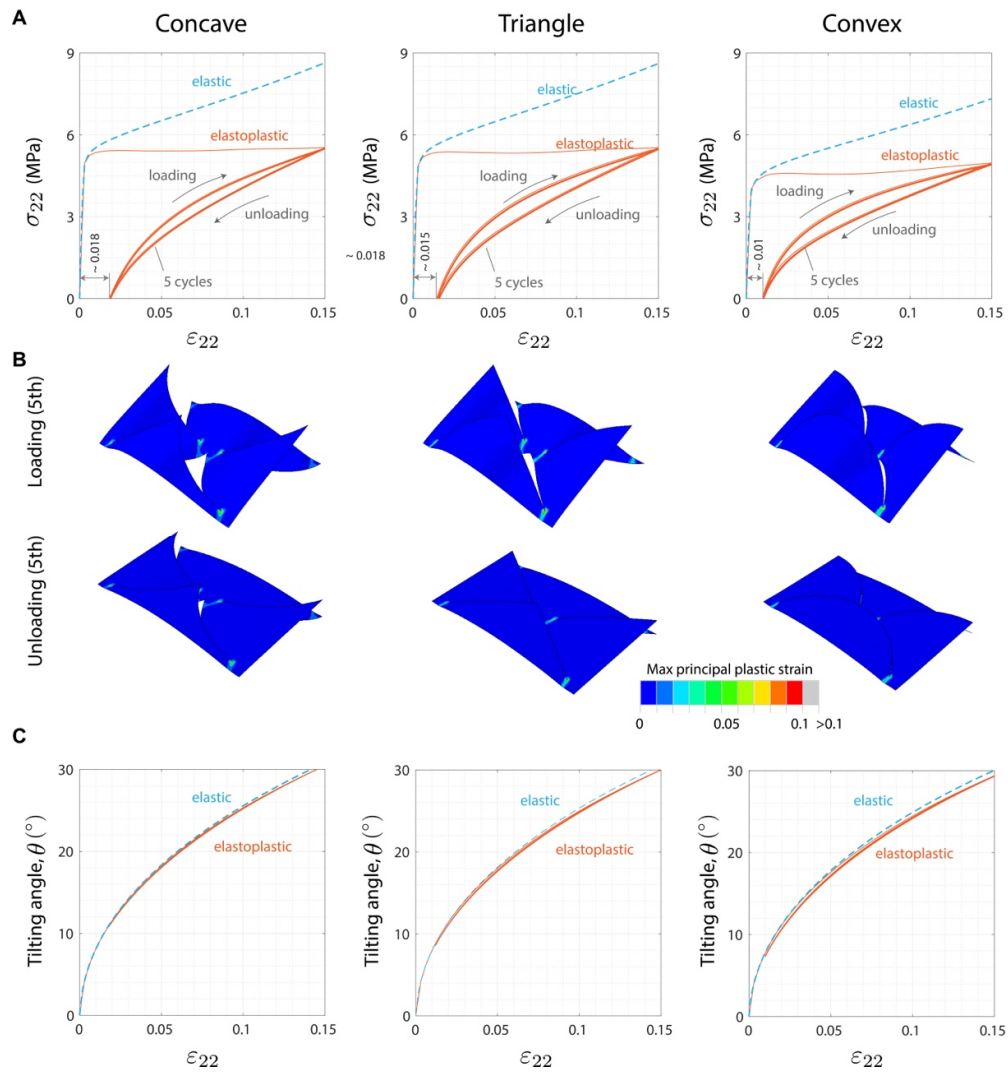


Fig. S10: Effect of material behavior on the response of kirigami structures subjected to uniaxial tension. (A) Comparison between numerical stress–strain curves obtained considering a purely elastic (blue dashed lines) and an elastoplastic (orange solid lines for five cyclic loads) material model. Results are reported for concave, triangle, and convex spike shapes steel kirigami patches, characterized by $\gamma = 30^\circ$, $\delta/l = 0.15$ with the residual macroscopic plastic strains 0.018, 0.015, and 0.010, respectively. (B) Snapshots showing the distribution of max principal plastic strains at buckled (loading at $\varepsilon_{22} = 0.15$) and released (unloading at $\varepsilon_{22} = 0$) configurations for 5 cyclic uniaxial tensile loads. (C) Comparison between the evolution of tilting angle of the spikes (θ) as a function of applied strain (ε_{22}) for a purely elastic (blue dashed lines) and an elastoplastic (orange solid lines for five cyclic loads) material model.

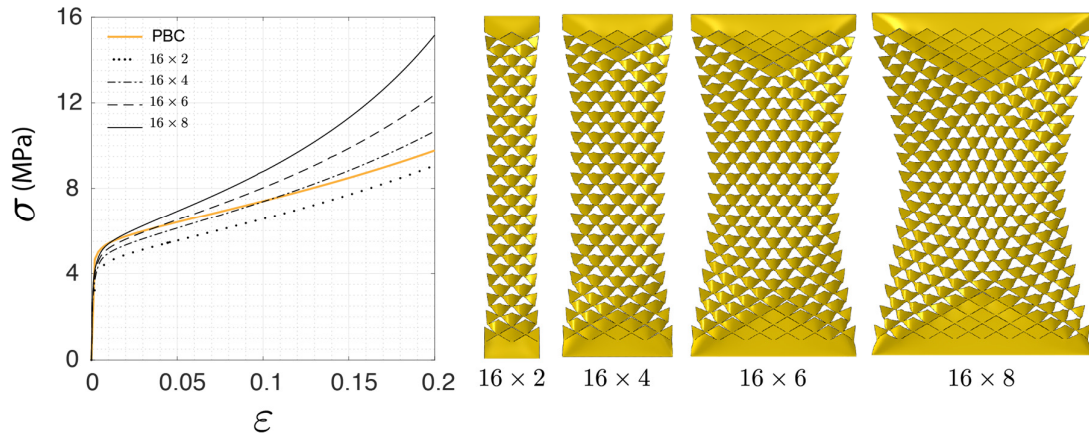


Fig. S11: Stress-strain response of the finite size kirigami under uniaxial tension. Comparison between the response of finite size samples (comprised of 16×2 , 16×4 , 16×6 , 16×8 units) and infinitely large periodic structure (PBC) under uniaxial tension for triangular cut pattern obtained from FEA.

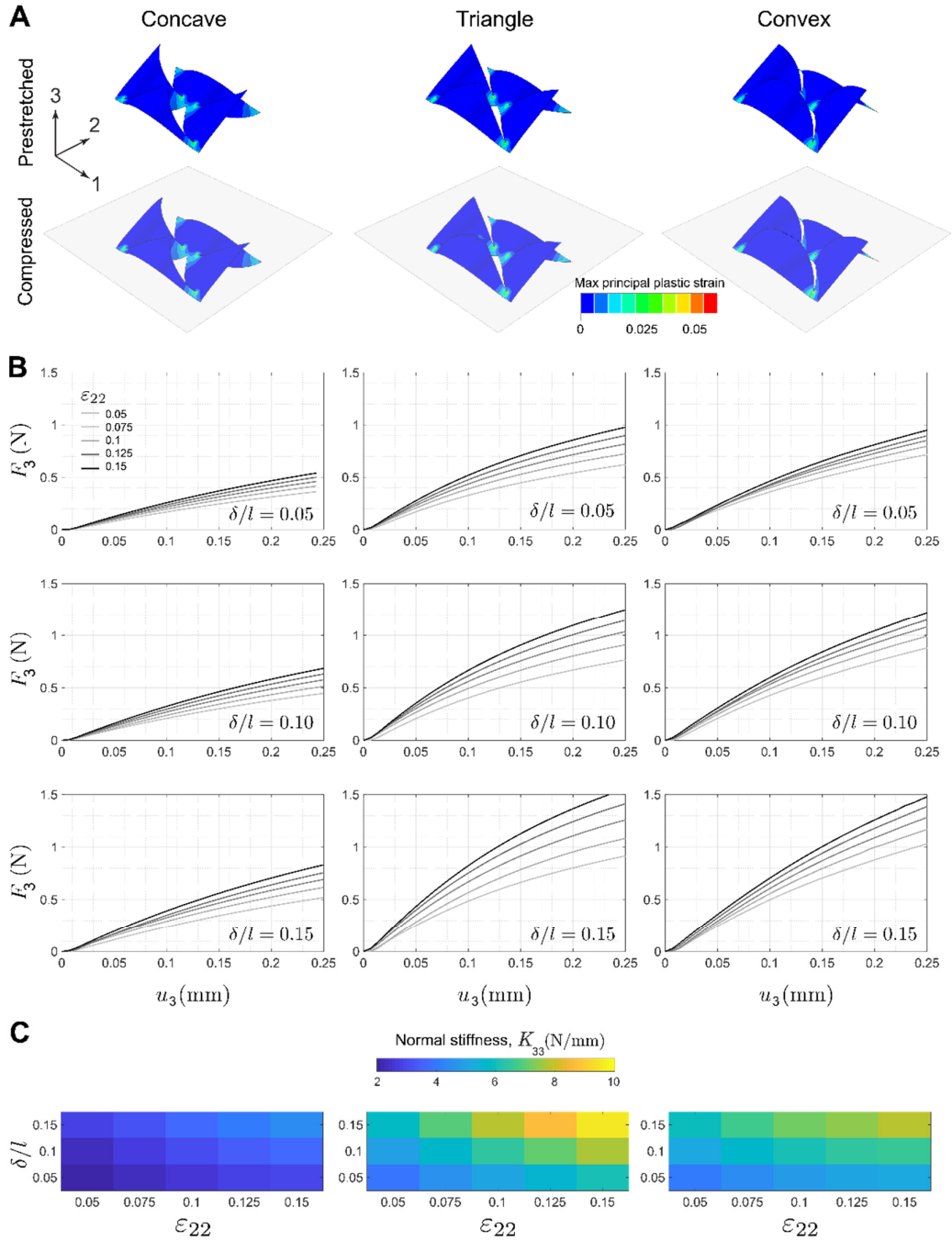


Fig. S12: Evolution of normal stiffness of the kirigami surfaces. (A) FEA simulation of periodic kirigami unit cells which are prestretched ($\epsilon_{22} = 0.15$) and subsequently compressed with a rigid plate. (B) Normal force-displacement curves for the different cut patterns and hinge width δ/l under different levels of applied strains ϵ_{22} . (C) Effect of δ/l on the stiffness in 33-direction (K_{33}) of the kirigami spikes with concave, triangle, and convex shapes with $\gamma = 30^\circ$ as a function of ϵ_{22} .

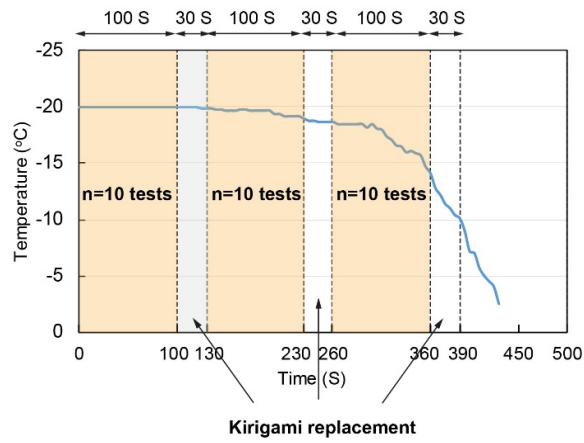


Fig. S13: Variation of ice surface temperature during human force plate measurement of friction with kirigami shoe grips. The temperature of ice blocks during the experiments was monitored using a K-type thermocouple embedded into the top surface. The average of temperature variations recorded over $t=7$ min for $n=30$ force-plate human tests (10 measurements per 100 S time periods with 30 S time interval between for replacing the kirigami shoe grips).

			P values
Fig. 3C Concave	Ice	μ_s (kirigami vs. control)	0.000912
		μ_k (kirigami vs. control)	0.000144
	Vinyl	μ_s (kirigami vs. control)	0.002367
		μ_k (kirigami vs. control)	0.032417
	Hardwood	μ_s (kirigami vs. control)	0.103851
		μ_k (kirigami vs. control)	0.000494
Fig. 3C Triangle	Ice	μ_s (kirigami vs. control)	0.023017
		μ_k (kirigami vs. control)	0.022258
	Vinyl	μ_s (kirigami vs. control)	0.093200
		μ_k (kirigami vs. control)	0.672700
	Hardwood	μ_s (kirigami vs. control)	0.031022
		μ_k (kirigami vs. control)	0.066804
Fig. 3C Convex	Ice	μ_s (kirigami vs. control)	0.015963
		μ_k (kirigami vs. control)	0.081590
	Vinyl	μ_s (kirigami vs. control)	0.002472
		μ_k (kirigami vs. control)	0.099844
	Hardwood	μ_s (kirigami vs. control)	0.026974
		μ_k (kirigami vs. control)	0.023503
Fig. 3F	Arrangement 1	μ_s (kirigami vs. control)	0.000912
		μ_k (kirigami vs. control)	0.000144
	Arrangement 2	μ_s (kirigami vs. control)	0.006200
		μ_k (kirigami vs. control)	0.001205
	Arrangement 3	μ_s (kirigami vs. control)	0.000134
		μ_k (kirigami vs. control)	0.000045
	Arrangement 4	μ_s (kirigami vs. control)	0.016297
		μ_k (kirigami vs. control)	0.022709
	Arrangement 5	μ_s (kirigami vs. control)	0.027102
		μ_k (kirigami vs. control)	0.010209

Table S1: Precise *P* values reported from the two-sample *t* tests used to determine the significance in Fig. 3.

Movie S1. Steel kirigami shoe grips attached to a shoe sole. The slip-resistant assistive kirigami metasurface attached to a shoe sole undergoes a shape transformation from a flat surface (corresponding to low friction) to the 3D textured surface with popped-up spikes (corresponding to high friction). This reversible shape transformation caused by bending of the shoe sole, which induces stretching in the patches, resulting in buckling out the spikes that enables us to tune friction actively and subsequent resistance to slips and falls.

Movie S2. Finite element simulation of kirigami unit cell. A periodic kirigami unit cell with concave spikes is initially stretched up to $\varepsilon_{22} = 0.15$ and then compressed in the normal direction by pushing down a rigid plate against it. The contours in top left panel shows distribution of max principal plastic strain during the deformation. The plastic strains localized in the hinges are moderate and the residual plastic strain is $\sim 2\%$.